

# 1 **First validation of GOME-2/MetOp Absorbing Aerosol Height using** 2 **EARLINET lidar observations**

3 **Konstantinos Michailidis<sup>1\*</sup>, Maria-Elissavet Koukouli<sup>1</sup>, Nikolaos Siomos<sup>1</sup>, Dimitrios Balis<sup>1</sup>, Olaf**  
4 **Tuinder<sup>2</sup>, L. Gijbert Tilstra<sup>2</sup>, Lucia Mona<sup>3</sup>, Gelsomina Pappalardo<sup>3</sup> and Daniele Bortoli<sup>4,5</sup>**

5 <sup>1</sup>Laboratory of Atmospheric Physics, Physics Department, Aristotle University of Thessaloniki, Greece

6 <sup>2</sup>Royal Netherlands Meteorological Institute (KNMI), De Bilt, the Netherlands

7 <sup>3</sup>Consiglio Nazionale delle Ricerche – Istituto di Metodologie per l'Analisi Ambientale (CNR-IMAA), C. da S. Loja,  
8 TitoScalo (PZ), Italy

9 <sup>4</sup>Institute of Earth Sciences (ICT), Évora, Portugal

10 <sup>5</sup>Physics Department, University of Évora, Portugal

11 *Correspondence to:* Konstantinos Michailidis (komichai@physics.auth.gr)

12 **Abstract.** The aim of this study is to investigate the potential of the GOME-2 instruments on board the MetOpA, MetOpB  
13 and MetOpC platforms, to deliver accurate geometrical features of lofted aerosol layers. For this purpose, we use archived  
14 ground-based lidar data from stations available from the European Aerosol Research Lidar Network (EARLINET)  
15 database. The data are post-processed using the wavelet covariance transform (WCT) method in order to extract  
16 geometrical features such as the Planetary Boundary Layer (PBL) height and the cloud boundaries. To obtain a significant  
17 number of collocated and coincident GOME-2 – EARLINET cases for the period between January 2007 and September  
18 2019, thirteen lidar stations, distributed over different European latitudes, contributed to this validation. For the 172  
19 carefully screened collocations, the mean bias was found to be  $-0.18 \pm 1.68$  km, with a near Gaussian distribution. On a  
20 station-basis, and with a couple of exceptions where very few collocations were found, their mean biases fall in the  $\pm 1$  km  
21 range with an associated standard deviation between 0.5 and 1.5 km. Considering the differences, mainly due to the  
22 temporal collocation and the difference, between the satellite pixel size and the point view of the ground-based  
23 observations, these results can be quite promising and demonstrate that stable and extended aerosol layers as captured by  
24 the satellite sensors, are verified by the ground-based data. We further present an in-depth analysis of a strong and long-  
25 lasting Saharan dust intrusion over the Iberian Peninsula. We show that, for this well-developed and spatially well-spread  
26 aerosol layer, most GOME-2 retrievals fall within 1 km of the exactly temporally collocated lidar observation for the entire  
27 range of 0 to 150 km radii. This finding further testifies to the capabilities of the MetOp-born instruments to sense the  
28 atmospheric aerosol layer heights.

## 29 **1. Introduction**

30 Aerosols are important constituents of the atmosphere, influencing both the air quality and the Earth's climate. They scatter  
31 and absorb solar and terrestrial radiation (direct effect) can act as cloud condensation nuclei (CCN) in liquid water clouds  
32 (Bougiatioti et al., 2016; Georgoulias et al., 2020) and as ice-nucleating particles (INPs) in mixed-phase and ice clouds  
33 (indirect effect) (Seinfeld et al., 2016). Changes in their concentration affect cloud extent, lifetime, particle size and  
34 radiative properties (e.g. Ansmann et al., 2019; Laaksonen et al., 2020). However, the overall uncertainties in the radiative  
35 forcing effect of aerosols (anthropogenic and natural) remain still very high (IPCC, 2014). These uncertainties can only be

1 reduced by better quantifying the vertical and horizontal distribution of aerosols over several stations. Knowledge of  
2 geometrical features of aerosol layers is essential for understanding the impact of aerosols on the climate system. The  
3 aerosol height quantification of smoke, dust, biomass burning aerosols as well as volcanic ash, is a critical determinant of  
4 global aerosol transport and dispersion (Balis et al., 2016; Ansmann et al., 2018; Nanda et al., 2020; Sun et al, 2020). The  
5 spatial and temporal variation aerosol layer height is associated with the major aerosol sources and the atmospheric  
6 dynamics. Aerosol vertical distributions are affected by aerosol emissions and deposition processes, aerosol microphysical  
7 properties, meteorological conditions and chemical processes. Lidar aerosol vertical profiles provide an important means of  
8 evaluating and improving aerosol models. Atmospheric aerosol models are generally sensitive in the vertical  
9 distribution of aerosols with large regional variability (Kipling et al., 2016). In the framework of aviation safety,  
10 it is important to have accurate knowledge about the height of aerosol layers in the atmosphere since dust, biomass burning  
11 and ash particles can be transported over large distances away from their source and so global monitoring is essential (e.g.  
12 Pappalardo et al., 2010, 2013; Balis et al., 2016; Soupiona et al., 2020; Adam et al., 2020).

13 There are several differences in the sensing principles between active and passive remote sensing of aerosols, specifically  
14 in terms of the vertical resolution. Lidar (Light detection and ranging) remote sensing techniques can provide accurate  
15 vertical profiles of the aerosol backscatter and extinction coefficients, which are representative of aerosol load, with vertical  
16 resolution of a few meters (Papayannis et al., 2008). Active remote - sensing instruments, like lidars - that are part of the  
17 European Aerosol Research Lidar Network (EARLINET; Pappalardo et al, 2014), have been used to distinguish between  
18 different aerosol types by providing vertical profiles of aerosol optical properties, as well to understand the three-  
19 dimensional structure and variability in time of the aerosol field (e.g. Amiridis et al., 2015; Ansmann et al., 2018; Voudouri  
20 et al., 2019). Although they provide great details in the vertical direction, lidar measured aerosol profiles are subjected to  
21 limited spatial and temporal coverage. On the other hand, passive spaceborne remote sensing instrumentation has the ability  
22 to measure a specific point on Earth once a day for polar orbiting satellite missions and several times in the day for  
23 geostationary missions. Polar satellites such as the Meteorological Operational satellite programme (MetOp) series offer the  
24 advantage of global and daily coverage and instruments such as Global Ozone Monitoring Experiment-2 (GOME-2) have  
25 already been used for aerosol detection (Hassinen et al., 2016). Therefore, combined studies based on ground-based lidars  
26 together with atmospheric satellites will allow full exploitation of this data for a detailed description of the temporal and  
27 spatial distribution and evolution on a global scale.

28 The only way to obtain the temporal and spatial variations of aerosol profiles on global scale is through the satellite  
29 remote sensing. Passive satellite remote sensing of aerosol layer height can by far not provide the same details as active  
30 remote sensing techniques but adds an important extension compared to active remote sensing in terms of spatial coverage.  
31 spaceborne lidars, such as CALIOP onboard CALIPSO (Winker et al., 2009), provide measurements of high spatial and  
32 temporal distributions of aerosol and clouds and their geometrical and optical properties (Vaughan et al., 2009). While  
33 CALIOP has excellent vertical resolution and has the ability to resolve the layer heights of multiple plumes in a single  
34 profile, its swath width is very narrow and has a 16d global coverage compared to the passive sensors, which have daily  
35 global coverage. Several previous studies, different algorithms and sensitivities analyses have employed a variety of  
36 definitions of the aerosol height from passive instruments until now (Sun et al., 2019). Some important mentions of

1 missions for aerosol layer height (ALH) retrieval are: the Ozone Monitoring Instrument (OMI) on board the NASA Aura  
2 satellite (Chimot et al., 2018), the Multi-angle Imaging SpectroRadiometer (MISR) on board the NASA Terra satellite  
3 (Nelson et al., 2013), the Deep Space Climate Observatory (DSCOVR) mission with its Earth Polychromatic Imaging  
4 Camera (EPIC) (Xu et al., 2019) and currently the TROPOspheric Monitoring Instrument (TROPOMI) instrument on board  
5 the Sentinel-5 Precursor satellite (Veefkind et al., 2012). The next years, missions like the upcoming Tropospheric  
6 Emissions: Monitoring Pollution mission (TEMPO) (Zoogman et al., 2017) and the Multi-Angle Imager for Aerosols  
7 (MAIA) mission (Davis et al., 2017) are expected to provide aerosol height retrievals as well. These instruments are  
8 examples of missions demonstrably more capable of retrieving Aerosol layer height.

9  
10 In this study, a quantitative assessment of Level 2 absorbing aerosol height product derived by the GOME-2 aboard the  
11 MetOp platforms (Munro et al. 2016; Hassinen et al., 2016), using EARLINET lidar data as reference. Furthermore a case  
12 study with several MetOp overpasses close to the EARLINET station of Évora, Portugal, (38.56°N, -7.91°E, 293m a.s.l) on  
13 20-23 February 2017, is analyzed to demonstrate the performance of the GOME-2 Absorbing Aerosol Height (AAH)  
14 retrieval for a strong Saharan dust event. This paper is organized as follows. In Sect. 2, the GOME-2/MetOp satellite-borne  
15 instrument and the European Aerosol Research Lidar Network (EARLINET) are described. The data and methodology are  
16 briefly described in Section 3. In Sect. 4, the network-based intercomparison results between GOME-2 and EARLINET and  
17 a selected dust case are presented. Finally, Section 5 contains the summary and the conclusions of this article.

## 18 **2. Satellite and ground-based instrumentation**

### 19 **2.1 Description of the GOME-2 instrument**

20 The Global Ozone Monitoring Instrument (GOME-2) instrument, on board the MetOp-A, B and C platforms, is a UV–VIS–  
21 NIR (visible–near IR) nadir viewing scanning spectrometer, with an across-track scan time of 6s and a nominal swath width  
22 of 1920 km, which provides global coverage of the sunlit part of the atmosphere within a period of approximately 1.5 days  
23 (Hassinen et al., 2016; Munro et al., 2016). The MetOp satellite series is the core element of the European Organization for  
24 the Exploitation of Meteorological Satellites (EUMETSAT) Polar System (EPS), developed in partnership with the  
25 European Space Agency (ESA). The primary GOME-2 instrument onboard MetOps perform equally and main  
26 characteristics are listed in Table 1. The three GOME-2 instruments provide unique and long data sets for atmospheric  
27 research and applications. The complete mission time is expected to cover 2007-2024 period. The AC SAF (Satellite  
28 Application Facility on Atmospheric composition) is responsible for the development and distribution of the GOME-2  
29 Level 2 products accessed through the AC SAF web portal, [https://acsaf.org/product\\_list.html](https://acsaf.org/product_list.html).

### 30 **2.2 The EARLINET network**

31 The EARLINET network was founded in 2000 as a research project for establishing a quantitative, comprehensive, and  
32 statistically significant database for the horizontal, vertical, and temporal distribution of aerosols on a continental scale  
33 (Bösenberg et al., 2003; Pappalardo et al., 2014). Since then EARLINET has continued to provide the most extensive  
34 collection of ground-based data for the aerosol vertical distribution over Europe. EARLINET is one of the components of

1 ACTRIS, the European Aerosol Clouds and Trace gases Research Infrastructure, now in its implementation phase. Within  
2 ACTRIS, many developments have been realized in EARLINET improving the quality assurance of the lidar systems and  
3 the quality control procedures of the lidar data (e.g. Freudenthaler et al., 2016, 2018). Additionally improvements in  
4 retrieved products as well as advanced products have been developed through integration with observations from other  
5 ACTRIS components. The SCC is a major component of the ACTRIS Aerosol Remote Sensing Node (ARES) responsible  
6 for the curation and the processing of the ACTRIS aerosol remote sensing data (D'Amico et al., 2015; Mattis et al., 2016).

7 The geographical distribution of the lidar stations can be found at the EARLINET website  
8 (<https://www.earlinet.org/index.php?id=105>). Aerosol lidar observations in the framework of EARLINET are performed  
9 according to a common schedule and on preselected dates. The schedule involves three measurements per week, namely  
10 one during daytime at around local noon on Monday at 14:00±1 UTC and two during nighttime on Monday and Thursday  
11 at sunset +2/3 h to enable Raman extinction retrievals. Furthermore, observations are devoted to monitoring special events  
12 over the continent, such as Saharan dust outbreaks, forest fires, photochemical smog, and volcanic eruptions (e.g. Balis et  
13 al., 2003; Amiridis et al., 2009; Sicard et al., 2011; Pappalardo et al., 2013; Fernández et al., 2018; Soupiona et al., 2018,  
14 2019, 2020). EARLINET observations have already been used for climatological studies (e.g. Giannakaki et al.; 2010;  
15 Siomos et al. 2018), long-range transport analysis (Ansmann et al., 2003; Papayannis et al., 2008), aerosol characterization  
16 of dust forecast modeling (Perez et al., 2006; Mona et al., 2012; Mona et al. 2014), among others. Furthermore, retrieval  
17 algorithms related to aerosol microphysical properties were developed with real multi-wavelength lidar data (Müller et al.  
18 2007; Tesche et al, 2009; Balis et al., 2010; Mamouri et al., 2012). So far, EARLINET represents an available tool for  
19 validation and exploitation of data from the Cloud-Aerosol Lidar and Infrared Pathfinder Satellite Observation (CALIPSO;  
20 Winker et al., 2009) mission and several studies have investigated the CALIPSO products (e.g., Mamouri et al. 2009; Mona  
21 et al., 2009; Pappalardo et al. 2010; Amiridis et al., 2015; Papagiannopoulos et al., 2016). Also, the multiwavelength  
22 EARLINET data will be very useful for the validation of current and future satellite missions, such as the ESA Explorer  
23 missions Atmospheric Dynamics Mission – Aeolus (ADM-Aeolus), Sentinel-5 Precursor (S5-P), Earth Clouds, Aerosols  
24 and Radiation Explorer (EarthCARE).

25 Some of the EARLINET systems perform 24/7 continuous measurements as, for example, the PollyXT systems (Baars et  
26 al., 2016; Engelmann et al., 2016). It hence follows that EARLINET consists of rather different lidar systems regarding the  
27 number of measured wavelengths and signal channels, the detection range, which is mainly determined by laser power and  
28 telescope size and number, the optical design and the electronic signal detection techniques. The majority of EARLINET  
29 stations are equipped with multi-wavelength Raman channels and many of them operate depolarization channels that  
30 measure the depolarization of the emitted linearly polarized radiation. In order to ensure qualitative and consistent data  
31 processing within the EARLINET network, algorithm intercomparison campaigns have been organized (e.g. Pappalardo et  
32 al., 2004, Wandinger et al., 2016, Amodeo et al., 2018). These campaigns aimed to assure the homogeneity of the data  
33 despite the differences in the lidar systems of the stations.

### 1 **3. Data and Methodology**

#### 2 **3.1 Satellite data (GOME-2)**

##### 3 **3.1.1 Absorbing Aerosol Index (AAI)**

4 The Absorbing Aerosol Index (AAI) indicates the presence of elevated amounts of absorbing aerosols in the Earth's  
5 atmosphere. Is a unitless index and separates the spectral contrast at two ultraviolet (UV) wavelengths (340/380nm) caused  
6 by aerosol scattering and absorption from other effects, including molecular Rayleigh scattering, surface reflection and  
7 gaseous absorption (Torres et al., 1998). The aerosol types that are mostly seen in the AAI are desert dust and biomass  
8 burning aerosols. Absorbing aerosol index is a unitless parameter, with higher values indicating elevated amount of aerosols  
9 present in the atmosphere. Negative values are caused by the presence of clouds and/or scattering aerosol in the scene.  
10 However a positive value for the AAI can only be explained by the presence of absorbing aerosols. The paper of de Graaf et  
11 al. (2005) provides several sensitivity analyses that detail the importance of the aerosol height for the interpretation of the  
12 AAI. The AAI from GOME-2 is produced by the Royal Netherlands Meteorological Institute, KNMI, -within the  
13 framework of the AC SAF. The GOME-2 AAI products are calculated for all three MetOp-A, MetOp-B and MetOp-C  
14 satellite instruments and data are available since January 2007, December 2012 and January 2019, respectively (ACSAF:  
15 <https://acsaf.org/datarecords/aai.html>, KNMI: <http://www.temis.nl/airpollution/absaai/>)

##### 16 **3.1.2 Absorbing Aerosol Height (AAH)**

17 The AAH is a new operational ACSAF EUMETSAT product for aerosol layer height detection, developed by KNMI within  
18 the AC SAF. It uses the Absorbing Aerosol Index (AAI) as an indicator to derive the actual height of the absorbing aerosol  
19 layer in the O2-A band using the Fast Retrieval Scheme for Clouds Observables (FRESCO) algorithm (Wang et al. 2008,  
20 2012; Tilstra et al., 2010, 2012). The retrieved aerosol height varies from the bottom to the top of the aerosol layer,  
21 depending on the aerosol optical thickness (AOT), solar zenith angle (SZA) and actual aerosol layer top height (Wang et al.,  
22 2008). The AAH product can be used to monitor volcanic eruptions globally and provide the height of the ash layers (Balis  
23 et al., 2016). The Absorbing Aerosol Height is very sensitive to cloud contamination. However, aerosols and clouds can  
24 prove difficult to distinguish and AAH is computed for different FRESCO cloud fractions. Not only FRESCO is able to  
25 determine the height of an absorbing aerosol layer in the absence of clouds, but under certain conditions also in the  
26 presence of clouds. Further details and more information associated with the AAH product, are available in the Product  
27 User Manual (PUM) and Algorithm Theoretical Basis Document (ATBD; Tilstra et al. 2019, PUM; Tilstra et al., 2020). The  
28 product is available openly from the ACSAF repository, [https://acsaf.org/offline\\_access.html](https://acsaf.org/offline_access.html), and has been officially  
29 validated (De Bock, et al., 2020). As discussed in the ATDB, observation pixels with AAI values below 2.0 correspond to  
30 scenes with too low amount levels of aerosol to result in a reliable AAH retrieval. Also for AAI values larger than 2.0 but  
31 smaller than 4.0 the aerosol layer is not in all cases thick enough for a reliable retrieval. However, most of our aerosol cases  
32 correspond to AAI values below the 4.0 level. The AAH product is provided, among others, with the related standard  
33 deviation value. In summary, the AAH algorithm retrieves, from the GOME-2 level-1b Product, the following parameters  
34 CF (effective aerosol/cloud fraction), CH (aerosol/cloud height), SA (scene albedo), SH (scene height). Two different  
35 aerosol/cloud layer heights (CH and SH) are determined by the AAH algorithm. It is up to the algorithm to decide which of

1 the two is the best candidate to represent the actual AAH level. According to Wang et al. (2012) in order to distinguish  
2 whether the contribution of clouds is crucial, three situations about the reliability of the AAH product are used and the  
3 effective cloud fraction (CF) is used to check in which of these regimes is the better solution (A: High reliability, B:medium  
4 reliability, C:Low reliability). In more detail:

- 5 ▪ **Regime A** ( $CF \leq 0.25$ ) refers to the situation in which there is either only a low degree of cloud cover or the aerosol  
6 optical depth is sufficiently large to compensate the presence of a cloud layer below the aerosol layer. Exceptions are  
7 cases with low aerosol amounts, but these scenes were filtered out beforehand by demanding that the AAI must be  
8 higher than a threshold AAI value.
- 9 ▪ **Regime B** ( $0.25 < CF < 0.75$ ) is an intermediate regime and the AAH found this way is likely to underestimate the AAH  
10 in some cases, and the reliability attributed to this regime is medium.
- 11 ▪ **Regime C** ( $CF \geq 0.75$ ) is the situation of a thick cloud layer present in the scene. In this case an aerosol layer is only  
12 retrieved successfully when the aerosol layer is sufficiently thick. The reliability is therefore characterized as low. More  
13 information can found in Wang et al. (2012)

14  
15 In the Sect. 3.3, a pie chart (cf. Fig. 6) with the distribution of reliability category (Regimes) of collocated observations is  
16 presented, including the contribution of clouds.

### 17 3.2 Ground-based lidar data (EARLINET)

18 The EARLINET database represents the largest collection of ground-based data of the vertical aerosol distribution on a  
19 continental scale. EARLINET members, as well as external users, get access to the database through a web interface  
20 ([www.earlinet.org](http://www.earlinet.org); Last access: 23 April 2020). Additionally EARLINET data are permanently indexed and published at  
21 WDCC (<https://www.earlinet.org/index.php?id=247>). The main information stored in the files of the EARLINET database  
22 is the vertical distribution of aerosol backscatter and extinction coefficients. Additionally, there are more optional variables  
23 included in the files, such as the lidar ratio, the particle linear depolarization ratio and the water vapor mixing ratio profiles.  
24 In this study, we use the backscatter profiles for aerosol layer height retrieval. The backscatter files contain at least a profile  
25 of the aerosol backscatter coefficient ( $m^{-1}sr^{-1}$ ) derived from the elastic backscatter signal and may be accompanied by an  
26 extinction coefficient profile. Here, we use the vertical information of backscatter profiles (at 1064nm and 532nm in some  
27 cases) for selected EARLINET stations. Quality assurance (QA) tests have been established and software intercomparison  
28 campaigns (Wandinger et al., 2016; Freudenthaler et al., 2018) have been organized in the framework of EARLINET in order  
29 to assure the homogeneity of the data despite the differences in the lidar systems of the stations. A list of the EARLINET  
30 stations used for the validation of GOME-2 AAH and their geographical coordinates are given in Table 2 and presented in  
31 Fig.1. The stations are located such that four European regions are covered: Central Europe, Western Mediterranean,  
32 Central Mediterranean and eastern Mediterranean. In this way, a large variety of aerosol optical and geometrical  
33 characteristics can be investigated.

### 3.2.1 Wavelet covariance transform (WCT) method

In this section we analyze the algorithmic processes that are required to extract geometrical features from lidar signals employed in this work. The aerosol geometrical properties carry information about the structure of lidar profiles, such as the boundary layer height and the features of the lofted aerosol layers and can be obtained from any lidar profile. In this study a full lidar dataset from thirteen EARLINET stations has been used for the calculations. Some lidar optical products however are more reliable to use than others. For example, the longer wavelengths typically magnify the differences in the vertical distribution of the aerosol load, resulting in layers that are easier to identify. Furthermore, the Raman inversion always results in profiles that are less structured for the extinction coefficients than the backscatter coefficients. This is the reason why we prioritize them so as to produce geometrical properties (Baars et al., 2008; Siomos et al., 2017). The product with the highest potential to magnify the aerosol layer structure available is selected for each measurement. More specifically, the backscatter products are prioritized over the extinction products and the longer wavelengths over the shorter ones. For this study, backscatter profiles at 1064 nm have been chosen primarily, and in some cases backscatter profiles at 532 nm.

The wavelet-covariance transform (WCT) technique has proved to be one of the most reliable methods for the PBL top detection. Many methods have been proposed for the calculation of the PBL height from lidar data (e.g., Flamant et al., 1997; Brooks, 2003; Banks et al., 2016; Kokkalis et al., 2020). Our analysis is based on the method of Baars et al. (2008) that applies the wavelet covariance transform (WCT) to the raw lidar data in order to extract geometrical features such as the PBL height, aerosol and cloud boundaries. The WCT transformation has also been applied successfully in the past on other lidar products (e.g. R.E. Kalman, 1960; Rocardendosch et al., 1999). Siomos et al. (2017), for example, use an adaptation of the WCT method to calculate the geometrical features from the aerosol concentration profiles. The wavelet covariance transform was defined as a means of detecting step changes in a signal. It is based upon a compound step function, the Haar function  $h$ , defined as shown in Eq. (1):

$$h\left(\frac{z-b}{a}\right) = \begin{cases} +1: b - \frac{a}{2} \leq z \leq b \\ -1: b \leq z \leq b + \frac{a}{2} \\ 0: elsewhere, \end{cases} \quad (1)$$

Here,  $h[(z-b)/a]$  is the Haar function,  $a$  is the dilation of the Haar function indicating the size of the window (or dilation),  $b$  is the center of the Haar function (or the translation) and  $z$  is the altitude range. The covariance transform of the Haar function,  $W_f(a, b)$ , is defined as shown in Eq. (2):

$$W_f(a, b) = a^{-1} \int_{z_0}^{z_1} f(z) h\left(\frac{z-b}{a}\right) dz \quad (2)$$

where  $f(z)$  is the backscatter lidar signal,  $z_b$  and  $z_t$  are the lowest altitude and the highest altitude of possible layers heights. The  $W_f(a, b)$  is referred to as the wavelet coefficient. These variables define the window function. Based on the

1 defined lower and upper limits the Haar transform is calculated. The obtained Haar values are subjected to the covariance  
2 transform and the maximum negative value of the covariance transform provides the aerosol layer top. The key issues of  
3 performing the WCT are the determination of the dilation value of the Haar function. As with previous studies (Brooks et  
4 al., 2003; Baars et al., 2008), the dilation factor  $a$ , affects the number of covariance wavelet transform coefficient local  
5 minima. Larger values of dilation factor reveal a few large local minima, at the height of the biggest aerosol loading in the  
6 aerosol backscatter profile. In addition, lower dilation values, create local minima at heights of smaller aerosol loads in the  
7 profiles. A dilation of 0.5 km is used in this study for the lofted aerosol layer height calculations. An example of a lidar  
8 backscatter profile with resulting WCT profile from the Barcelona lidar station (Universitat Politècnica de Catalunya,  
9 Barcelona – UPC) on June 29, 2019 is given in Fig.2. This figure is reasonably to show the ability of the lidar to detect  
10 multiple layers. The blue lines refer to S-G (Savitzky – Golay smoothed signal) and the yellow one to the noisy backscatter  
11 lidar signal. The horizontal red dashed line represents the detected aerosol layer top applying the WCT methodology (see  
12 the section 3.2.1) and three aerosol layers are detected, according the methodology that we follow. Applying the WCT we  
13 can check if there are strong variations in the backscatter coefficient profile within an aerosol layer, which may lead to a  
14 classification of a separate layer. The colored “star” symbols represent the local maxima (purple) and minima (red) of  
15 wavelet transform signal.

### 17 **3.3 Validation methodology and collocation criteria**

18 The validation of products with a typical resolution of several kilometers against point-like ground-based measurements  
19 involves uncertainties. A key question is how well the ground-based observation represents a larger area around the  
20 measurement site and to a large extent depends on the characteristics of the station location (urban, sub-urban, etc). In this  
21 study, to obtain a significant number of collocated GOME-2 – EARLINET cases, data from thirteen EARLINET stations  
22 were used for the GOME-2 AAH product validation as shown in Table 2. As the UV-VIS satellite instruments provide  
23 daytime observations, only the lidar measurements temporally close to the satellite overpass are used in this comparison. To  
24 achieve a good agreement between retrieved aerosol height from O2-A band observations and ground-based lidar  
25 measurements is very challenging and depends on some assumptions (Sanders et al., 2015). The lidar backscatter profiles  
26 are used to retrieve aerosol layer height (ALH) information of the aerosol vertical profile, while the AAH product is  
27 extracted by the GOME-2 algorithm. For the comparison of GOME-2 AAH against aerosol height from EARLINET lidars,  
28 the coincidence criteria are set to a 150 km search radius between the satellite pixel center and the geolocation of the  
29 ground-based station. The lidar measurements nearest to the GOME-2 overpass time within a 5 hour temporal interval were  
30 selected for every available day of measurement, to ensure a sufficiently large collocation database. It should also be noted  
31 that the temporal criterion is necessary since most of the EARLINET lidar observations occur at noon or night while the  
32 MetOp orbits are in the morning. For each ground-based measurement, only the spatially closest GOME-2 measurements  
33 were selected for the comparison study.

34 Furthermore, certain criteria for ensuring the quality and representativeness of the satellite measurements, such as sun  
35 glint, solar eclipse events, and AAI values greater than 2 were taken into account. In this study, we use only the pixels  
36 containing positive AAI values, corresponding to absorbing aerosols, and especially only values greater (or equal) than 2.0.

1 According to Tilstra et al. (ATBD, 2019) observation pixels with AAI values below 2.0 correspond to scenes with too low  
2 amount levels of aerosol to result in a reliable AAH retrieval. This threshold, does not apply to every passive satellite  
3 instrument which retrieve the aerosol layer height product. For example, the TROPOMI ALH is only retrieved for pixels  
4 with UV AI (calculated by 354-388nm wavelength pair) larger than 1. In addition, unconverging pixels with AAH set to be  
5 15 km are also excluded. Due to the use of FRESCO algorithm, GOME-2 is limited to a maximum height of 15km for the  
6 AAH retrieval and hence cannot detect layers higher than 15km. Table 3 lists the GOME-2 quality-assurance thresholds  
7 applied in the EARLINET comparison. Selecting these criteria, the total set of available satellite pixels is quite small. Most  
8 of the satellite measurements available from GOME-2 / MetOp refer to cases with AAI between 2 and 4.

9 Applying all these selection criteria resulted in a total of 272 correlative GOME-2 – EARLINET cases suitable for the  
10 comparison study and representativeness of the GOME-2 Level-2 AAH product. However, it quickly became clear that  
11 further consideration of the individuality of each sensing instrument is required. A large amount of GOME-2 AAH heights  
12 below the 1km level are reported, which in most cases are unlikely to be retrieved from a lidar backscatter profile due to the  
13 system overlap (Wandinger and Ansmann, 2002). This is a common source of uncertainty when dealing with lidar data, due  
14 to hardware limitations, that determine the altitude above which a profile contains trustworthy values. This is demonstrated  
15 in the 0-1 km bin of Fig.3, where the collocations are separated depending on the AAH reported per instrument. Most of the  
16 vertical lidar profiles begin over 0.8-1.0 km and is indeed quite rare to find profiles starting below of these values.  
17 Therefore in this study, a threshold value of 1.0 km, for the signal altitude is selected, under which we will not take into  
18 account observations in our analysis. The backscatter profiles archived in the EARLINET database have a variable height  
19 range which typically extends up to 5-6 km where the most of the lidar signals have an optimal signal-to-noise ratio.  
20 Therefore, as can also be seen for the last bar – for heights above 6km - (cf. Fig. 3), there are very few cases where the  
21 lidars report heights above that altitude. Collocated cases where the lidar ALH values are greater than 7 km, have been  
22 removed from the study.

23 As a result of this extra restriction in collocation, the number of GOME-2 – EARLINET cases considered in the  
24 assessment of the accuracy and representativeness of the GOME-2 AAH are provided in Table 2 including the code name of  
25 the EARLINET station used in figures further in the text. Figure 4 (left panel) shows the distribution of available of  
26 collocated cases for each lidar station and in Fig.4 (right panel) the distribution of all collocations by year. All three GOME-  
27 2 instruments are considered in one single satellite data pool. Figure 5 shows the spatial distribution of all collocated layers  
28 around each EARLINET station considered (Athens, Barcelona, Belsk, Bucharest, Granada, Évora, Lecce, Limassol,  
29 Minsk, Potenza, Sofia, Thessaloniki and Warsaw) while the concentric red circles denote regions of 150 km from the  
30 location of these stations. In Fig.6 the distribution of reliability category (Regime) of collocated observations is presented,  
31 including the contribution of clouds. The effective cloud fraction (CF) is a primary indicator for the AAH algorithm and is  
32 used to check which of these regimes is more reliable for retrieving the AAH. It is clear that most of the collocated cases  
33 belong to the high (regime A) and medium (regime B) reliability categories. We take into account all the Regime flags of  
34 pixels regardless of the reliability. According to Wang et al. (2012), Regime C is the situation of a thick cloud layer present  
35 in the scene. In this case, an aerosol layer is only retrieved successfully when the aerosol layer is sufficient thick.

## 1 **4. Results**

### 2 **4.1 GOME-2 & EARLINET comparison statistics**

3 In this section an overall assessment of the GOME-2 retrieved AAH product is given, using the total dataset of GOME-2 –  
4 EARLINET collocated cases. In Figure 7 shows the distribution of GOME-2 AAH and EARLINET aerosol height  
5 differences. The histogram plot refers to the total of 172 collocated cases. The near Gaussian distribution of the absolute  
6 difference is centered slightly to the left, indicating lower GOME-2 AAH values on average with a mean bias of -0.18 km  
7 and standard deviation of 1.68 km, a very promising result considering all the individual uncertainties of both datasets as  
8 well as the collocation criteria. The related metrics are given in Table 4. Fig.8 shows the updated bar plot, effectively  
9 demonstrating the reason for the lingering differences between the two datasets. A comparison for all study stations can be  
10 seen in Fig.9 where the collocations are now color-coded per their associated AAI value. The overall agreement is quite  
11 satisfactory with most lidar AAH values between 1 and 7 km, while the GOME-2 AAH results range a bit higher up to ~8  
12 km. The individual station statistics are given in Table 5, sorted by the number of collocations found for each station. The  
13 mean bias (GOME-2 AAH – EARLINET ALH) falls well within the  $\pm 1$  km range, with an associated standard deviation  
14 between 0.5 and ~2 km. Considering the differences mainly in the temporal collocation and the difference between the  
15 satellite pixel size and the point view of the ground-based observations, these results are quite promising as the stable  
16 aerosol layers are well captured by the satellite sensors.

17 Some of the lingering differences may be explained as follows: as per Fig.3, the geometrical and technical characteristics  
18 of each lidar system determine the height range where backscatter profiles can be retrieved, and this can affect the  
19 comparisons at very low and very high ALHs. Additionally, GOME-2 AAH retrieval assumes a single aerosol layer in the  
20 atmospheric column, while it is a common feature to have more layers in the column. This is well captured by the lidar  
21 observations, but making the GOME-2 against lidar comparison there is some uncertainty which lidar derived layer should  
22 be compared to the GOME-2 equivalent one.

### 23 **4.2. Saharan dust outbreak event between 21-23 February 2017**

24 An intense Saharan dust episode occurred between the 20<sup>st</sup> -23<sup>rd</sup> of February over the Iberian Peninsula. Analysis of the  
25 meteorological conditions during this dust event are described in Fernández et al (2018). In this section we present the  
26 evolution of the dust outbreak event that was captured by the Évora, Portugal, lidar station between the 21<sup>st</sup> and the 23<sup>rd</sup> of  
27 February 2017 as well as the GOME-2 AAH observations.

#### 28 **4.2.1 Évora lidar station**

29 This Évora station is located about 100 km eastward from the Atlantic west ocean. Due to its geographical location Évora is  
30 influenced by different aerosol types namely urban as well as mineral and forest fire aerosol particles. The lidar system here  
31 installed (PAOLI-Portable Aerosol and Cloud Lidar), is a multi-wavelength Raman lidar belonging to the Polly<sup>XT</sup> family  
32 (Baars et al., 2016) with high temporal and spatial resolution, operating since September 2009. It is installed at the Évora  
33 Atmospheric Science's Observatory (EVASO) and operated by the University of Évora (UE) and the Institute of Earth  
34 Sciences (ICT) (38.56°N, -7.91°E, 293 m a.s.l).The instrument features three elastic channels in the UV-VIS-IR range (355,

1 532 and 1064nm), two inelastic (Raman) channels (387 and 607nm) and a polarization channel which detects the cross  
2 polarized signal at 532nm. PAOLI is participating both in the EARLINET and the Spanish and Portuguese Aerosol Lidar  
3 Network, SPALINET (Sicard et al., 2009 and 2011). The Évora lidar system, being part of EARLINET, has been quality-  
4 assured through direct inter-comparisons, both at hardware (Matthias et al., 2004) and algorithm levels (Böckmann et al.,  
5 2004; Pappalardo et al., 2004). During daytime, data provided by the Klett technique (Klett, 1981, 1985) use as input a  
6 constant lidar ratio value to retrieve the backscatter coefficient values with an average uncertainty of the order of 20–30%  
7 (Pappalardo et al., 2014).

#### 8 **4.2.2 Case study: Évora, 21-23 February 2017**

9 In February 2017, an exceptionally extreme event affected the whole Iberian Peninsula, as examined with AERONET,  
10 EARLINET lidars and passive-satellite observations (Fernández et al. 2018). MetOp overpasses close to the EARLINET  
11 station of Évora are analyzed here to demonstrate the performance of the GOME-2 instrument under the intense Saharan  
12 dust outbreak (see Fig.13). This typical case concerns an intense Saharan dust outbreak, which lasted for three days (21 to  
13 23 February 2017) and was successfully followed during these three days by the Évora lidar station. A combined use of  
14 lidar profiles, back-trajectory analysis, dust models and satellite observations allows the identification of Saharan dust  
15 cases. Fig.10 shows the temporal evolution of the aerosol total attenuated backscatter coefficient at 1064nm ( $\text{m}^{-1}\text{sr}^{-1}$ ) over  
16 Évora on 21-23 February.

17 In order to verify the origin of the aerosol layers, observed by the ground-based lidar and GOME-2/MetOp satellite, we  
18 calculated backward air-mass trajectories by using the HYSPLIT model (Hybrid Single-Particle Lagrangian Integrated  
19 Trajectory, available online at <http://ready.arl.noaa.gov/HYSPLIT.php>) through the READY system on the site of Air  
20 Resource Laboratory, ARL, of NOAA, USA (National Oceanic and Atmospheric Administration) (Stein et al., 2015; Rolph  
21 et al., 2017). GDAS (Global Data Analysis System) meteorological files with a spatial resolution of  $1^\circ \times 1^\circ$  every 3 h,  
22 generated and maintained by ARL, are used as data input. The calculations of backward air mass trajectories show the  
23 provenance of the air mass traversed for a chosen time period before arriving at Évora at 10:00 UTC. The temporal  
24 evolution of five days backward trajectories, from 21 to 23 February 2017 for arrival heights 1000 m (red), 2000 m (blue)  
25 and 3500 m (green) to cover the height range of the observed layers that we recognize in structures of height time displays  
26 of the range-corrected lidar signal, is shown in Fig.11. The trajectory analysis reveals that the origin of aerosol air masses is  
27 indeed the Sahara desert.

28 In Fig.12, satellite maps from the Moderate resolution Imaging Spectroradiometer (MODIS, Levy et al., 2013), an  
29 instrument aboard the Terra satellite, show the dust being transported by air masses over the Atlantic before returning  
30 towards Portugal and Spain on the 21<sup>st</sup> (Fig.12, panel a), 22<sup>nd</sup> (Fig.12, panel b) and 23<sup>rd</sup> (Fig.12, panel c) of February 2017.  
31 To illustrate the evaluation methodology for the GOME-2 Level 2 AAH, a pair of collocated and concurrent GOME-2 and  
32 EARLINET lidar observations is shown in Fig.13. We apply the proposed methodology in the measurement performed at  
33 the morning of 23<sup>rd</sup> of February 2017. The case study was selected as a large set of GOME-2 AAH retrieved pixels is  
34 available and extremely high values of AAI are observed indicating the large aerosol dust load during this day. The  
35 retrieved absorbing aerosol height pixels are shown in Fig.13 (panel b, d) and the retrieved AAI in Fig.13 (panel a, c). Data

1 gaps in the maps represent screened-out bright pixels due to either cloud or pixels affected by the sun glint effect while  
2 recall that AAH retrievals are only available when AAI is  $\geq 2$ . We will examine this date in particular later on as the  
3 extremely high AAI values, as well as the direct temporal morning collocations, give us confidence in the resulting  
4 comparisons.

5 As previously mentioned, both ground-and satellite-based followed this major dust event for all three days of February  
6 2017. An example of the equivalent backscatter profiles observed by EARLINET station and the information about  
7 coincidence of AAH measured by GOME-2 are reported in Fig. 15. The horizontal dashed blue lines in the left plots  
8 column indicate the AAH value derived from the centered GOME-2 pixel. Additional information such as the absorbing  
9 aerosol height (AAH), aerosol height error, absorbing aerosol index (AAI), cloud fraction (CF) and distance of collocated  
10 centered GOME-2 pixels from EARLINET station are displayed as legend. On the 21<sup>st</sup> of February, a well-defined aerosol  
11 layer is picked up by the lidar at 10:01:23 UT (Fig.14, panel a) spanning between 1.5 and 3 km. The collocated GOME-2B  
12 observation between 09:59 and 10:30 UTC, at a distance of 62.7 km from the ground station, has an associated AAI value  
13 of 2.65, cloud fraction of 10% and an AAH estimate at 2.07 km (blue dashed line), well within the range seen by the lidar at  
14 the surface. For the case of the 22<sup>nd</sup> of February, the aerosol layer appears to split into two separate plumes (Fig.14, panel  
15 c), with GOME-2A reporting an AAI value of 2.07, i.e. quite close to the threshold value of 2.0. Even though the cloud  
16 fraction remains low ( $\sim 10\%$ ), the satellite AAH estimate is quite low (0.8 km). On the 23<sup>rd</sup> of February, (Fig.14, bottom)  
17 GOME-2B reports a pixel quite close to the station, at 25 km, and even though the reported AAH of 2.8 km (dashed blue  
18 line) is well within the range of the aerosol layer height reported by the lidar, the high cloud fraction of 45% and associated  
19 extreme AAI value of 5.75 makes it difficult to draw further conclusions. In Fig.15, we show the comparisons for all  
20 GOME-2 pixels against the simultaneous lidar observation for the 23<sup>rd</sup> of February, over Évora station. The collocated  
21 points are color-coded by their associated AAI value. In this way, we can assess whether the general agreement shown by  
22 the collocations of Fig. 13, can be turned into a generalized comment as to behavior of the GOME-2 AAH algorithm for  
23 cases of high AAI and good temporal collocations. Due to the sufficient amount of collocations in this case study, only  
24 observations with AAI larger than 4 are shown. The spread of the satellite estimates are within  $\pm 1$  km from the lidar  
25 observations (red and green dashed lines) for the vast majority of the cases shown, for all spatial distances between ground  
26 and satellite pixel. The results of this study case could be also interpreted taking into account the representativeness study  
27 done using EARLINET and CALIPSO data (Pappalardo et al., 2010) during an intense dust case in 27–30 May 2008. The  
28 agreement seems to decrease with larger distances and this follows the losing of correlation between observation when the  
29 distance from station increasing. Additionally at the same study, Pappalardo et al. (2010) demonstrate that at 100 km  
30 maximum horizontal distance, the variability is strong already with time differences larger than 1 hour, so probably this is  
31 the reason of the observed differences between satellite and ground based observations. These results further strengthens  
32 our original assessment that the satellite algorithm is mature enough to observe stable and homogeneously-distributed  
33 aerosol layers in the troposphere.

## 5. Summary and conclusions

In this paper, we presented the first validation results of GOME-2/MetOp AAH product using lidar data from EARLINET database. For this scope, lidar backscatter profiles at 1064nm have been chosen primarily, and in some cases backscatter profiles at 532nm. -. The total number of carefully screened collocations with the EARLINET lidar measurements was 172 for the three GOME-2 instruments aboard on MetOpA, MetOpB and MetOpC, between 2007 and 2019. A wide choice of lidar stations around Europe was made in order to examine the behavior of the comparisons for different typical common aerosol load over the locations; South European stations are often affected by Saharan dust intrusions, Central European stations are further affected by local and transboundary pollution events of both anthropogenic and natural origin and Northern European stations are mostly free of dust and most sense particle of anthropogenic provenance. A spatial collocation criterion of 150 km, and temporal of 5h, were selected, so as to obtain a sufficient amount of collocations. The official lidar EARLINET dataset has been post-reprocessed by an automatic geometrical feature detection algorithm, known as the WCT algorithm. The WCT method make use of the elastic backscattered coefficient at 532 and 1064nm in combination with criteria flags. This method can be only applied in stations with at least one elastically resolved backscatter profile. The results of this article encourages the operational usage of the WCT-based algorithms in validation processes. The inter-comparison results are very promising, showing that the GOME-2 AAH measurements provide a good estimation of the aerosol layer altitudes sensed by the lidar ground-based instruments. On average, the mean absolute bias (GOME-2 minus lidar height) was found to be  $-0.18 \pm 1.68$  km, with a near Gaussian distribution and minimum and maximum differences between  $\sim \pm 5$  km. On a station-basis, and with a couple of exceptions, their mean biases fall in the  $\pm 1$  km range with an associated standard deviation between 0.5 and 2 km. Considering the differences, mainly due to the temporal collocation and the difference between the satellite pixel size and the point view of the ground-based observations, these results are quite promising and demonstrate that stable aerosol layers are well captured by the satellite sensors. The official AC SAF requirements on the accuracy of the GOME-2 AAH product state that, for heights  $< 10$  km, the threshold accuracy is 3 km, the target accuracy is 2 km and the optimal accuracy is 1 km. This validation effort shows that for all cases the target accuracy is achieved, and for specific aerosol heights, also the optimal, well within user requirements.

An extreme Saharan dust event, which advected large dust loads from the North African continent over Iberian Peninsula on 21-23 February, 2017, was analyzed in detailed. In this case, numerous collocations were found within  $\pm 30$ min with the Évora, Portugal, lidar system. This permitted a more stringent criterion on the Absorbing Aerosol Index, AAI, to be used, permitting collocations with associated  $AAI > 4$  to be considered. This validation effort shows that for all cases the target accuracy is achieved, and for well-developed and spatially well-spread aerosol layers, GOME-2 retrievals meet also the optimum user requirements for the aerosol layer height of 1km. This finding further testifies to the capabilities of the MetOp-born instruments to sense the atmospheric aerosol layer height. EARLINET represents an optimal tool to validate satellite instruments data and to provide necessary information to fully exploit the data produced. Furthermore, the EARLINET network is a suitable database to contribute also to future passive satellite missions such as the TROPOspheric Monitoring Instrument (TROPOMI S-5P; Veefkind et al., 2012) on board the Sentinel-5 Precursor (S5P) satellite, for the validation of aerosol layer height products.

1 **Author Contributions:** KM carried out the processing of satellite and lidar measurements and prepared the figures of the  
2 manuscript. MEK and DB were responsible for the methodology and conceptualization of the paper. GP and LM ensured  
3 the provision of the QA EARLINET data. OT and LGT were responsible to provide satellite data, detailed description and  
4 use of the GOME-2 Absorbing Aerosol Height product. NS contributed to the development of automatic algorithm for the  
5 aerosol layer detection using lidar data. DB reviewed the case study of the Évora EARLINET station, as presented in the  
6 paper. KM prepared the manuscript with contributions from all co-authors.

7  
8 **Data availability.** The data of the GOME-2 Absorbing Aerosol Height (AAH) product are provided by KNMI in the  
9 framework of the EUMETSAT Satellite Application Facility on Atmospheric Composition Monitoring (AC SAF). GOME-2  
10 AAI browse images are freely distributed via the TEMIS website at <http://www.temis.nl>. EARLINET aerosol profile data  
11 are reported in the EARLINET Data base: <https://data.earlinet.org>, and are accessible from its repository and from the  
12 ACTRIS Data Portal (<http://actris.nilu.no>). The data policy of these data is harmonized with the ACTRIS data policy. The  
13 authors gratefully acknowledge the NOAA Air Resources Laboratory (ARL) for the provision of the HYSPLIT transport  
14 and dispersion model and/or READY website <https://www.ready.noaa.gov> used in this publication.

15  
16 **Competing interests.** The authors declare that they have no conflict of interest.

17  
18 **Acknowledgments.** The authors would like to thank the PIs of all EARLINET stations and their staff for establishing and  
19 maintaining the EARLINET sites and for the provision of ground-based lidar data used in this paper. The data of the  
20 GOME-2 Absorbing Aerosol Index are provided by KNMI in framework of the EUMETSAT Satellite Application Facility  
21 on Atmospheric Composition (AC SAF). The authors acknowledge EARLINET for providing aerosol lidar profiles  
22 available at <https://data.earlinet.org/>. We further acknowledge the support of this work by the project “PANhellenic  
23 infrastructure for Atmospheric Composition and climatE change” (MIS 5021516) which is implemented under the Action  
24 “Reinforcement of the Research and Innovation Infrastructure”, funded by the Operational Programme "Competitiveness,  
25 Entrepreneurship and Innovation" (NSRF 2014-2020) and co-financed by Greece and the European Union (European  
26 Regional Development Fund). The work is partially supported by the ACTRIS-2 project, funded from the European Union’s  
27 Horizon 2020 research and innovation programme (grant agreement No. 654109) and by ACTRIS-IMP (Implementation  
28 project), funded in the frame of the programme H2020 Grant Agreement 871115. The work is partially supported by the  
29 European Union through the European Regional Development Fund, included in the COMPETE 2020 (Operational  
30 Program Competitiveness and Internationalization) through the ICT project (UIDB/04683/2020) with the reference POCI-  
31 01-0145- FEDER-007690 and also through TOMAQAPA (PTDC/CTAMET/ 29678/2017)

## 32 33 **References**

34 Adam, M., Nicolae, D., Stachlewska, I. S., Papayannis, A., and Balis, D.: Biomass burning events measured by lidars in  
35 EARLINET – Part 1: Data analysis methodology, *Atmos. Chem. Phys.*, 20, 13905–13927, [https://doi.org/10.5194/acp-20-](https://doi.org/10.5194/acp-20-13905-2020)  
36 13905-2020, 2020.

1  
2 Amiridis, V., Balis, D. S., Giannakaki, E., Stohl, A., Kazadzis, S., Koukouli, M. E., and Zanis, P.: Optical characteristics of  
3 biomass burning aerosols over Southeastern Europe determined from UV-Raman lidar measurements, *Atmos. Chem.*  
4 *Phys.*, 9, 2431–2440, doi:10.5194/acp-9-2431-2009, 2009.

5 Amiridis, V., E. Marinou, A. Tsekeri, U. Wandinger, A. Schwarz, E. Giannakaki, R. Mamouri, P. Kokkalis, I. Biniotoglou, S.  
6 Solomos, T. Herekakis, S. Kazadzis, E. Gerasopoulos, D. Balis, A. Papayannis, C. Kontoes, K. Kourtidis, N.  
7 Papagiannopoulos, L. Mona, G. Pappalardo, O. Le Rille, and A. Ansmann: LIVAS: a 3-D multi-wavelength  
8 aerosol/cloud climatology based on CALIPSO and EARLINET, *Atmos. Chem. Phys.*, 15, 7127-7153, doi:10.5194/  
9 acp-15-7127-2015, 2015

10 Amodeo A, D’Amico G, Giunta A, Papagiannopoulos N, Papayannis A, Argyrouli A, Mylonaki M, TsaknakisG, Kokkalis P,  
11 Soupiona R, Tzanis C (2018) ATHLI16: the ATHens lidar intercomparison campaign. In: 28th international laser radar  
12 conference, 25–30 June 2017, Bucharest, Romania, 176:09008.https://doi.org/10.1051/epjconf/201817609008

13 Ansmann, A., et al., Long-range transport of Saharan dust to northern Europe: The 11 – 16 October 2001 outbreak observed  
14 with EARLINET, *J. Geophys. Res.*, 108(D24), 4783, doi:10.1029/2003JD003757, 2003

15 Ansmann, A., Baars, H., Chudnovsky, A., Mattis, I., Veselovskii, I., Haarig, M., Seifert, P., Engelmann, R., and Wandinger,  
16 U.: Extreme levels of Canadian wildfire smoke in the stratosphere over central Europe on 21–22 August 2017, *Atmos.*  
17 *Chem. Phys.*, 18, 11831–11845, https://doi.org/10.5194/acp-18-11831-2018, 2018.

18 Ansmann, A., Mamouri, R.-E., Bühl, J., Seifert, P., Engelmann, R., Hofer, J., Nisantzi, A., Atkinson, J. D., Kanji, Z. A.,  
19 Sierau, B., Vrekoussis, M., and Sciare, J.: Ice-nucleating particle versus ice crystal number concentration in  
20 altocumulus and cirrus layers embedded in Saharan dust: a closure study, *Atmos. Chem. Phys.*, 19, 15087–  
21 15115, https://doi.org/10.5194/acp-19-15087-2019, 2019.

22 Baars, H., Ansmann, A., Engelmann, R., and Althausen, D.: Continuous monitoring of the boundary-layer top with lidar,  
23 *Atmos. Chem. Phys.*, 8, 7281–7296, https://doi.org/10.5194/acp-8-7281-2008, 2008.

24 Baars, H., Kanitz, T., Engelmann, R., Althausen, D., Heese, B., Komppula, M., Preißler, J., Tesche, M., Ansmann,  
25 A., Wandinger, U., Lim, J.-H., Ahn, J. Y., Stachlewska, I. S., Amiridis, V., Marinou, E., Seifert, P., Hofer, J., Skupin,  
26 A., Schneider, F., Bohlmann, S., Foth, A., Bley, S., Pfüller, A., Giannakaki, E., Lihavainen, H., Viisanen, Y., Hooda,  
27 R. K., Pereira, S. N., Bortoli, D., Wagner, F., Mattis, I., Janicka, L., Markowicz, K. M., Achtert, P., Artaxo, P.,  
28 Pauliquevis, T., Souza, R. A. F., Sharma, V. P., van Zyl, P. G., Beukes, J. P., Sun, J., Rohwer, E. G., Deng, R.,  
29 Mamouri, R.-E., and Zamorano, F.: An overview of the first decade of PollyNET: an emerging network of  
30 automated Raman-polarization lidars for continuous aerosol profiling, *Atmos. Chem. Phys.*, 16, 5111–5137, https://  
31 doi.org/10.5194/acp-16-5111-2016, 2016.

32 Balis D., E. Giannakaki, D. Müller, V. Amiridis, K. Kelektoglou, S. Rapsomanikis and A. Bais, Estimation of the  
33 microphysical aerosol properties over Thessaloniki, Greece, during the SCOUT-O3 campaign with the synergy of  
34 Raman lidar and sunphotometer data, *J. of Geophys. Res.*, 115, D08202, doi:10.1029/2009JD013088, 2010.

35 Balis, D., Koukouli, M.-E., Siomos, N., Dimopoulos, S., Mona, L., Pappalardo, G., Marengo, F., Clarisse, L., Ventress, L.  
36 J., Carboni, E., Grainger, R. G., Wang, P., Tilstra, G., van der A, R., Theys, N., and Zehner, C.: Validation of ash

1 opticaldepth and layer height retrieved from passive satellite sensors using EARLINET and airborne lidar data: the  
2 case of the Eyjafjallajökull eruption, *Atmos. Chem. Phys.*, 16, 5705–5720, <https://doi.org/10.5194/acp-16-5705-2016>,  
3 2016.

4 Banks RF, Tiana-Alsina J, Baldasano JM, Rocadenbosch F, Papayannis A, Solomos S, Tzani CG: Sensitivity of boundary-  
5 layer variables to PBL schemes in the WRF model based on surface meteorological observations, lidar, and  
6 radiosondes during the HygrA-CD campaign. *Atmos Res* 176–177:185–  
7 201.<https://doi.org/10.1016/j.atmosres.2016.02.024>, 2016

8 Bougiatioti, A., Bezantakos, S., Stavroulas, I., Kalivitis, N., Kokkalis, P., Biskos, G., Mihalopoulos, N., Papayannis, A., and  
9 Nenes, A.: Biomass-burning impact on CCN number, hygroscopicity and cloud formation during summertime in the  
10 eastern Mediterranean, *Atmos. Chem. Phys.*, 16, 7389–7409, <https://doi.org/10.5194/acp-16-7389-2016>, 2016.

11 Brooks, I.M.: Finding Boundary Layer Top: Application of a Wavelet Covariance Transform to Lidar Backscatter Profiles,  
12 *J. Atmos.Ocean.Tech.*,20,1092–1105, [https://doi.org/10.1175/1520-0426\(2003\)020<1092:FBLTAO>2.0.CO;2](https://doi.org/10.1175/1520-0426(2003)020<1092:FBLTAO>2.0.CO;2), 2003.

13 aerosol backscatter data, *Atmos. Meas. Tech.*, 10, 1609–1622, <https://doi.org/10.5194/amt-10-1609-2017>, 2017.

14 Chimot, J., Veefkind, J. P., Vlemmix, T., and Levelt, P. F.: Spatial distribution analysis of the OMI aerosol layer height:  
15 a pixel-by-pixel comparison to CALIOP observations, *Atmos. Meas. Tech.*, 11, 2257–2277,  
16 <https://doi.org/10.5194/amt-11-2257-2018>, 2018.

17 D'Amico, G., Amodeo, A., Baars, H., Biniotoglou, I., Freudenthaler, V., Mattis, I., Wandinger, U., and Pappalardo, G.:  
18 EARLINET Single Calculus Chain – overview on methodology and strategy, *Atmos. Meas. Tech.*, 8, 4891-4916,  
19 [doi:10.5194/amt-8-4891-2015](https://doi.org/10.5194/amt-8-4891-2015), 2015

20 Davis, A. B., Kalashnikova, O. V., and Diner, D. J.: Aerosol Layer Height over Water from O2A-Band: Mono-Angle  
21 Hyperspectral and/or Bi-Spectral Multi-Angle Observations, <https://doi.org/10.20944/preprints201710.0055.v1>, 2017

22 De Bock, V., A. Declo, K. Michailidis, M. Koukoulis and D. Balis: SAF/AC VALIDATION REPORT, Absorbing Aerosol  
23 Height, SAF/AC/AUTH-RMI/VR/001, issue 1/2020, 03-07-20-2020,  
24 [https://acsaf.org/docs/vr/Validation\\_Report\\_AA\\_H\\_Jul\\_2020.pdf](https://acsaf.org/docs/vr/Validation_Report_AA_H_Jul_2020.pdf), last access: 15 October 2020.

25 De Graaf, M., Stammes, P., Torres, O., and Koелеmeijer, R. B. A.: Absorbing Aerosol Index: sensitivity analysis, application  
26 to GOME and comparison with TOMS, *J. Geophys. Res.*, 110,D01201, [doi:10.1029/2004JD005178](https://doi.org/10.1029/2004JD005178), 2005.

27 Engelmann, R., Kanitz, T., Baars, H., Heese, B., Althausen, D., Skupin, A., Wandinger, U., Komppula, M., Stachlewska, I.  
28 S., Amiridis, V., Marinou, E., Mattis, I., Linné, H., and Ansmann, A.: The automated multiwavelength Raman  
29 polarization and water-vapor lidar PollyXT: the neXT generation, *Atmos. Meas. Tech.*, 9, 1767–1784,  
30 [doi:10.5194/amt-9-1767-2016](https://doi.org/10.5194/amt-9-1767-2016), 2016

31 Fernández, A. J., Sicard, M., Costa, M. J., Guerrero-Rascado, J. L., Gómez-Amo, J. L., Molero, F., Barragán, R., Bortoli,  
32 D., Bedoya-Velásquez, A. E., Utrillas, M. P., Salvador, P., Granados-Muñoz, M. J., Potes, M., Ortiz-Amezcu, P.,  
33 Martínez-Lozano, J. A., Artíñano, B., Muñoz-Porcar, C., Salgado, R., Román, R., Rocadenbosch, F., Salgueiro, V.,  
34 Benavent-Oltra, J. A., Rodríguez-Gómez, A., Alados-Arboledas, L., Comerón, A., and Pujadas, M.: February 2017  
35 extreme Saharan dust outbreak in the Iberian Peninsula: from lidar-derived optical properties to evaluation of  
36 forecast models, *Atmos. Chem. Phys. Discuss.*, <https://doi.org/10.5194/acp-2018-370>, 2018.

- 1 Flamant, C., J. Pelon, P. H. Flamant, and P. Durand Lidar determination of the entrainment zone thickness at the top of the  
2 unstable marine atmospheric boundary layer. *Bound. Layer Meteor.*, 83, 247–284, 1997
- 3 Freudenthaler, V.: About the effects of polarising optics on lidar signals and the 490 calibration, *Atmos. Meas. Tech.*, 9,  
4 4181–4255, <https://doi.org/10.5194/amt-9-4181-2016>, 2016.
- 5 Freudenthaler, V., Linné, H., Chaikovski, A., Rabus, D., and Groß, S.: EARLINET lidar quality assurance tools, *Atmos.*  
6 *Meas. Tech. Discuss.*, <https://doi.org/10.5194/amt-2017-395>, in review, 2018.
- 7 Georgoulas A. K., Marinou E., Tsekeri A., Proestakis E., Akritidis D., Alexandri G., Zanis P., Balis D., Marengo F., Tesche  
8 M., and Amiridis V.: A first case study of CCN concentrations from spaceborne lidar observations, *Remote Sensing*,  
9 12(10), 1557, doi:10.3390/rs12101557, 2020.
- 10 Giannakaki, E., Balis, D. S., Amiridis, V., and Zerefos, C.: Optical properties of different aerosol types: seven years of  
11 combined Raman-elastic backscatter lidar measurements in Thessaloniki, Greece, *Atmos. Meas. Tech.*, 3, 569–578,  
12 <https://doi.org/10.5194/amt-3-569-2010>, 2010.
- 13 Hassinen, S., Balis, D., Bauer, H., Begoin, M., Delcloo, A., Eleftheratos, K., Gimeno Garcia, S., Granville, J., Grossi, M.,  
14 Hao, N., Hedelt, P., Hendrick, F., Hess, M., Heue, K.-P., Hovila, J., Jönch-Sørensen, H., Kalakoski, N., Kauppi, A.,  
15 Kiemle, S., Kins, L., Koukouli, M. E., Kujanpää, J., Lambert, J.-C., Lang, R., Lerot, C., Loyola, D., Pedergnana, M.,  
16 Pinardi, G., Romahn, F., van Roozendael, M., Lutz, R., De Smedt, I., Stammes, P., Steinbrecht, W., Tamminen, J.,  
17 Theys, N., Tilstra, L. G., Tuinder, O. N. E., Valks, P., Zerefos, C., Zimmer, W., and Zyrichidou, I.: Overview of the  
18 O3M SAF GOME-2 operational atmospheric composition and UV radiation data products and data availability,  
19 *Atmos. Meas. Tech.*, 9, 383–407, doi:10.5194/amt-9-383-2016, 2016
- 20 IPCC: Climate Change 2014, Synthesis Report, Contribution of Working Groups I, II and III to the Fifth Assessment Report  
21 of the Intergovernmental Panel on Climate Change, edited by: The Core Writing Team, Pachauri, R. K., and Meyer, L.  
22 A., IPCC, Geneva, Switzerland, available at: <http://www.ipcc.ch/report/ar5/syr/> (last access: 7 April 2019), 2014.
- 23 Kipling, Z., P. Stier, C.E. Johnson, G.W. Mann, N. Bellouin, S.E. Bauer, T. Bergman, M. Chin, T. Diehl, S.J. Ghan, T.  
24 Iversen, A. Kirkevåg, H. Kokkola, X. Liu, G. Luo, T. van Noije, K.J. Pringle, K. von Salzen, M. Schulz, Ø. Seland,  
25 R.B. Skeie, T. Takemura, K. Tsigaridis, and K. Zhang, 2016: What controls the vertical distribution of aerosol?  
26 Relationships between process sensitivity in HadGEM3-UKCA and inter-model variation from AeroCom Phase  
27 II. *Atmos. Chem. Phys.*, 16, 2221–2241, doi:10.5194/acp-16-2221-2016.
- 28 Klett, J.D.: Stable analytical inversion solution for processing lidar returns, *Appl. Opt.*, 20, 211–220,  
29 <https://doi.org/10.1364/AO.20.000211>, 1981.
- 30 Klett, J. D.: Stable analytic inversion solution for processing lidar returns, *Appl. Optics*, 20, 211–220, 1981. Klett, J. D.:  
31 Lidar inversion with variable backscatter/extinction ratios, *Appl. Optics*, 24, 1638–1643, 1985
- 32 Kokkalis, P., Alexiou, D., Papayannis, A. et al. Application and Testing of the Extended-Kalman-Filtering Technique for  
33 Determining the Planetary Boundary-Layer Height over Athens, Greece. *Boundary-Layer Meteorol* 176, 125–  
34 147, <https://doi.org/10.1007/s10546-020-00514-z>, 2020
- 35 Laaksonen, A., Malila, J., and Nenes, A.: Heterogeneous nucleation of water vapor on different types of black carbon  
36 particles, *Atmos. Chem. Phys.*, 20, 13579–13589, <https://doi.org/10.5194/acp-20-13579-2020>, 2020.

- 1 Levy, R. C., Mattoo, S., Munchak, L. A., Remer, L. A., Sayer, A. M., Patadia, F., and Hsu, N. C.: The Collection 6 MODIS  
2 aerosol products over land and ocean, *Atmos. Meas. Tech.*, 6, 2989– 3034, <https://doi.org/10.5194/amt-6-2989-2013>,  
3 2013.
- 4 Mamouri, R. E., Papayannis, A., Amiridis, V., Müller, D., Kokkalis, P., Rapsomanikis, S., Karageorgos, E. T., Tsaknakis, G.,  
5 Nenes, A., Kazadzis, S., and Remoundaki, E.: Multi-wavelength Raman lidar, sun photometric and aircraft  
6 measurements in combination with inversion models for the estimation of the aerosol optical and physico-chemical  
7 properties over Athens, Greece, *Atmos. Meas. Tech.*, 5, 1793–1808, doi:10.5194/amt-5-1793-2012, 2012
- 8 Mattis, I., D'Amico, G., Baars, H., Amodeo, A., Madonna, F., and Iarlori, M.: EARLINET Single Calculus Chain –  
9 technical – Part 2: Calculation of optical products, *Atmos. Meas. Tech.*, 9, 3009-3029, doi:10.5194/amt-9-3009-2016,  
10 2016
- 11 Mona, L., Pappalardo, G., Amodeo, A., D'Amico, G., Madonna, F., Boselli, A., Giunta, A., Russo, F., and Cuomo, V.: One  
12 year of CNR-IMAA multi-wavelength Raman lidar measurements in coincidence with CALIPSO overpasses: Level  
13 1 products comparison, *Atmos. Chem. Phys.*, 9, 7213–7228, <https://doi.org/10.5194/acp-9-7213-2009>, 2009.
- 14 Mona, L., Liu, Z., Müller, D., Omar, A., Papayannis, A., Pappalardo, G., Sugimoto, N. and Vaughan, M.: Lidar  
15 measurements for desert dust characterization: An overview, *Adv. Meteorol.*, 2012, doi:10.1155/2012/356265, 2012.
- 16 Mona, L., Papagiannopoulos, N., Basart, S., Baldasano, J., Binietoglou, I., Cornacchia, C., and Pappalardo, G.: EARLINET  
17 dust observations vs. BSC-DREAM8b modeled profiles: 12-year-long systematic comparison at Potenza, Italy,  
18 *Atmos. Chem. Phys.*, 14, 8781–8793, <https://doi.org/10.5194/acp-14-8781-2014>, 2014.
- 19 Müller, D., Ansmann, A., Mattis, I., Tesche, M., Wandinger, U., Althausen, D., and Pisani, G.: Aerosol-type-dependent lidar  
20 ratios observed with Raman lidar, *J. Geophys. Res.-Atmos.*, 112, D16202, <https://doi.org/10.1029/2006JD008292>,  
21 2007.
- 22 Munro, R., Lang, R., Klaes, D., Poli, G., Retscher, C., Lindstrot, R., Huckle, R., Lacan, A., Grzegorski, M., Holdak, A.,  
23 Kokhanovsky, A., Livschitz, J., and Eisinger, M.: The GOME-2 instrument on the Metop series of satellites:  
24 instrument design, calibration, and level 1 data processing – an overview, *Atmos. Meas. Tech.*, 9, 1279–1301,  
25 <https://doi.org/10.5194/amt-9-1279-2016>, 2016
- 26 Nanda, S., de Graaf, M., Veefkind, J. P., Sneep, M., ter Linden, M., Sun, J., and Levelt, P. F.: A first comparison of  
27 TROPOMI aerosol layer height (ALH) to CALIOP data, *Atmos. Meas. Tech.*, 13, 3043–  
28 3059, <https://doi.org/10.5194/amt-13-3043-2020>, 2020.
- 29 Nelson, D. L., Garay, M. J., Kahn, R. A., & Dunst, B. A. Stereoscopic height and wind retrievals for aerosol plumes with  
30 the MISR Interactive eXplorer (MINX). *Remote Sensing*, 5(9), 4593–4628. <https://doi.org/10.3390/rs5094593>, 2013
- 31 Papagiannopoulos, N., Mona, L., Alados-Arboledas, L., Amiridis, V., Baars, H., Binietoglou, I., Bortoli, D., D'Amico, G.,  
32 Giunta, A., Guerrero-Rascado, J. L., Schwarz, A., Pereira, S., Spinelli, N., Wandinger, U., Wang, X., and Pappalardo,  
33 G.: CALIPSO climatological products: evaluation and suggestions from EARLINET, *Atmos. Chem. Phys.*, 16, 2341–  
34 2357, <https://doi.org/10.5194/acp-16-2341-2016>, 2016.
- 35 Papayannis, A., Amiridis, V., Mona, L., Tsaknakis, G., Balis, D., Bösenberg, J., Chaikovski, A., De Tomasi, F., Grigorov, I.,  
36 Mattis, I., Mitev, V., Müller, D., Nickovic, S., Perez, C., Pietruczuk, A., Pisani, G., Ravetta, F., Rizi, V., Sicard,  
37 M., Trickl, T., Wiegner, M., Gerding, M., Mamouri, R.E., D'Amico, G., and Pappalardo, G.: Systematic lidar

1 observations of Saharan dust over Europe in the frame of EARLINET (2000–2002), *J. Geophys. Res.*, 113, D10204,  
2 doi:10.1029/2007JD009028, 2008.

3 Pappalardo, G., Amodeo, A., Pandolfi, M., Wandinger, U., Ansmann, A., Bösenberg, J., Matthias, V., Amiridis, V., De  
4 Tomasi, F., Frioud, M., Iarlori, M., Komguem, L., Papayannis, A., Rocadenbosch, F., and Wang, X.: Aerosol lidar  
5 intercomparison in the framework of the EARLINET project. 3. Raman lidar algorithm for aerosol extinction,  
6 backscatter and lidar ratio, *Appl. Optics*, 43, 5370–5385, 2004

7 Pappalardo, G., Wandinger, U., Mona, L., Hiebsch, A., Mattis, I., Amodeo, A., Ansmann, A., Seifert, P., Linné, H., Apitu  
8 ley, A., Alados Arboledas, L., Balis, D., Chaikovsky, A., D’Amico, G., De Tomasi, F., Freudenthaler, V., Gian nakaki,  
9 E., Giunta, A., Grigorov, I., Iarlori, M., Madonna, F., Mamouri, R., Nasti, L., Papayannis, A., Pietruczuk,  
10 A., Pujadas, M., Rizi, V., Roca-denbosch, F., Russo, F., Schnell, F., Spinelli, N., Wang, X., and Wiegner, M.: EAR  
11 LINET correlative measurements for CALIPSO: first intercomparison results, *J. Geophys. Res.*, 115, D00H19,  
12 doi:10.1029/2009JD012147, 2010

13 Pappalardo, G., Mona, L., D’Amico, G., Wandinger, U., Adam, M., Amodeo, A., Ansmann, A., Apituley, A., Alados  
14 Arboledas, L., Balis, D., Boselli, A., Bravo-Aranda, J. A., Chaikovsky, A., Comeron, A., Cuesta, J., De Tomasi, F.,  
15 Freudenthaler, V., Gausa, M., Giannakaki, E., Giehl, H., Giunta, A., Grigorov, I., Groß, S., Haeffelin, M., Hiebsch,  
16 A., Iarlori, M., Lange, D., Linné, H., Madonna, F., Mattis, I., Mamouri, R.-E., McAuliffe, M. A. P., Mitev, V.,  
17 Molero, F., Navas-Guzman, F., Nicolae, D., Papayannis, A., Perrone, M. R., Pietras, C., Pietruczuk, A., Pisani,  
18 G., Preißler, J., Pujadas, M., Rizi, V., Ruth, A. A., Schmidt, J., Schnell, F., Seifert, P., Serikov, I., Sicard, M.,  
19 Simeonov, V., Spinelli, N., Stebel, K., Tesche, M., Trickl, T., Wang, X., Wagner, F., Wiegner, M., and Wilson, K.  
20 M.: Four-dimensional distribution of the 2010 Eyjafjallajökull volcanic cloud over Europe observed by  
21 EARLINET, *Atmos. Chem. Phys.*, 13, 4429–4450, <https://doi.org/10.5194/acp-13-4429-2013>, 2013.

22 Pappalardo, G., Amodeo, A., Apituley, A., Comeron, A., Freudenthaler, V., Linné, H., Ansmann, A., Bösenberg, J.,  
23 D’Amico, G., Mattis, I., Mona, L., Wandinger, U., Amiridis, V., Alados-Arboledas, L., Nicolae, D., and Wiegner,  
24 M.: EARLINET: towards an advanced sustainable European aerosol lidar network, *Atmos. Meas. Tech.*, 7, 2389–  
25 2409, <https://doi.org/10.5194/amt-7-2389-2014>, 2014.

26 Pérez, C., Nickovic, S., Baldasano, J. M., Sicard, M., Rocadenbosch, F., and Cachorro, V. E.: A long Saharan dust event  
27 over the western Mediterranean: lidar, Sun photometer observations, and regional dust modeling?, *J. Geophys. Res.*,  
28 111, D15214, doi:10.1029/2005JD006579, 2006

29 R. E. Kalman, “A new approach to linear filtering and prediction problems,” *J. Basic Eng.* 82(1), 35–45, 1960

30 Rocadenbosch F., Soriano C., Comerón A., and Baldasano J., "Lidar inversion of atmospheric backscatter and extinction-to-  
31 backscatter ratios by use of a Kalman filter," *Appl. Opt.* 38, 3175-3189, 1999.

32 Rolph, G., Stein, A., and Stunder, B., (2017). Real-time Environmental Applications and Display sYstem: READY. *Envi  
33 ronmental Modelling & Software*, 95, 210-28, <https://doi.org/10.1016/j.envsoft.2017.06.025>, 2017

34 Sanders, A. F. J., de Haan, J. F., Sneep, M., Apituley, A., Stammes, P., Vieitez, M. O., Tilstra, L. G., Tuinder, O. N. E.,  
35 Koning, C. E., and Veeffkind, J. P.: Evaluation of the operational Aerosol Layer Height retrieval algorithm for Sentinel-  
36 5 Precursor: application to O2 A band observations from GOME-2A, *Atmos. Meas. Tech.*, 8, 4947–4977,  
37 <https://doi.org/10.5194/amt-8-4947-2015>, 2015.

1 Seinfeld, J. H., Bretherton, C. S., Carslaw, K. S., Coe, H., De- Mott, P. J., Dunlea, E. J., Feingold, G., Ghan, S. J., Guenther,  
2 A. B., Kahn, R. A., Kracunas, I. P., Kreidenweis, S. M., Molina, M. J., Nenes, A., Penner, J. E., Prather, K. A.,  
3 Ramanathan, V., Ramaswamy, V., Rasch, P. J., Ravishankara, A. R., Rosenfeld, D., Stephens, G., and Wood R.:  
4 Improving our fundamental understanding of the role of aerosol-cloud interactions in the climate system, *P. Natl.*  
5 *Acad. Sci. USA*, 113, 5781–5790, <https://doi.org/10.1073/pnas.1514043113>, 2016.

6 Sicard, M., Molero, F., Guerrero-Rascado, J. L., Pedros, R., Exposito, F. J., Cordoba-Jabonero, C., Bolarin, J. M., Comer  
7 on, A., Rocadenbosch, F., Pujadas, M., Alados-Arboledas, L., Martinez-Lozano, J. A., Diaz, J. P., Gil, M., Requena,  
8 A., Navas-Guzman, F., and Moreno, J. M.: Aerosol lidar intercomparison in the framework of SPALINET – the  
9 SPANish LIdar NETwork: methodology and results, *IEEE Trans. Geosci. Remote Sens.*, 47, 3547–3559, 2009.

10 Sicard, M., Pujadas, M., Alados-Arboledas, L., Pedros, R., Diaz, J. P., Cordoba-Jabonero, C., Requena, A., Comeron, A.,  
11 Rocadenbosch, F., Wagner, F., Rodrigues, J., Moreno, J. M.: SPALINET: The Spanish and Portuguese aerosol lidar  
12 network, *Opt. Pura Appl.*, 44, 1–5, 2011

13 Siomos, N.: Climatology and classification of the optical and microphysical properties of aerosols using ground – based  
14 remote sensing techniques (Doctoral dissertation), available at: <http://hdl.handle.net/10442/hedi/45104>, 2018

15 Siomos, N., Balis, D. S., Voudouri, K. A., Giannakaki, E., Filioglou, M., Amiridis, V., Papayannis, A., and Fragkos, K.: Are  
16 EARLINET and AERONET climatologies consistent? The case of Thessaloniki, Greece, *Atmos. Chem. Phys.*, 18,  
17 11885–11903, <https://doi.org/10.5194/acp-18-11885-2018>, 2018.

18 Siomos, N., Balis, D. S., Poupkou, A., Liora, N., Dimopoulos, S., Melas, D., Giannakaki, E., Filioglou, M., Basart, S., and  
19 Chaikovsky, A.: Investigating the quality of modeled aerosol profiles based on combined lidar and sunphotometer  
20 data, *Atmos. Chem. Phys.*, 17, 7003–7023, <https://doi.org/10.5194/acp-17-7003-2017>, 2017.

21 Stein, A.F., Draxler, R.R., Rolph, G.D., Stunder, B.J.B., Cohen, M.D., and Ngan, F. NOAA’s HYSPLIT atmospheric trans  
22 port and dispersion modeling system, *Bull. Amer. Meteor. Soc.*, 96, 2059-2077, <http://dx.doi.org/10.1175/BAMS->  
23 [D-14-00110.1](http://dx.doi.org/10.1175/BAMS-D-14-00110.1), 2015

24 Soupiona, O., Papayannis, A., Kokkalis, P., Mylonaki, M., Tsaknakis, G., Argyrouli, A. and Vratolis, S.: Long-term  
25 systematic profiling of dust aerosol optical properties using the EOLE NTUA lidar system over Athens, Greece (2000–  
26 2016), *Atmos. Environ.*, 183 (April), 165–174, doi:10.1016/j.atmosenv.2018.04.011, 2018.

27 Soupiona, O., Samaras, S., Ortiz-Amezcuca, P., Böckmann, C., Pa-payannis, A., Moreira, G. A., Benavent-Oltra, J. A.,  
28 Guerrero-Rascado, J. L., Bedoya-Velásquez, A. E., Olmo, F. J., Román,R., Kokkalis, P., Mylonaki, M., Alados-  
29 Arboledas, L., Papanikolaou, C. A., and Foskinis, R.: Retrieval of optical and micro-physical properties of transported  
30 Saharan dust over Athens and Granada based on multi-wavelength Raman lidar measurements: Study of the mixing  
31 processes, *Atmos. Environ.*, 214, 116824, <https://doi.org/10.1016/j.atmosenv.2019.116824>, 2019.

32 Soupiona, O., Papayannis, A., Kokkalis, P., Foskinis, R., Sánchez Hernández, G., Ortiz-Amezcuca, P., Mylonaki, M.,  
33 Papanikolaou, C.-A., Papagiannopoulos, N., Samaras, S., Groß, S., Mamouri, R.-E., Alados-Arboledas, L., Amodeo,  
34 A., and Psiloglou, B.: EARLINET observations of Saharan dust intrusions over the northern Mediterranean region  
35 (2014–2017): properties and impact on radiative forcing, *Atmos. Chem. Phys.*, 20, 15147–15166,  
36 <https://doi.org/10.5194/acp-20-15147-2020>, 2020.

- 1 Sun, J., Veefkind, P., Nanda, S., van Velthoven, P. and Levelt, P.: The role of aerosol layer height in quantifying aerosol  
2 absorption from ultraviolet satellite observations, *Atmos. Meas. Tech. Discuss.*, 1–24, doi:10.5194/amt-2019-96, 2019.
- 3 Sun, J., Veefkind, J. P., van Velthoven, P., Tilstra, L. G., Chimot, J., Nanda, S., and Levelt, P. F.: Defining aerosol layer  
4 height for UVAI interpretation using aerosol vertical distributions characterized by MERRA-2, *Atmos. Chem. Phys.*  
5 *Discuss.*, <https://doi.org/10.5194/acp-2020-39>, in review, 2020.
- 6 Tesche, M., Müller, D., Ansmann, A., Hu, M., Zhang, Y. H. Retrieval of microphysical properties of aerosol particles from  
7 one-wavelength Raman lidar and multiwavelength Sun photometer observations, *Atmos. Env.*, 42, 6398-6404,  
8 <https://doi.org/10.1016/j.atmosenv.2008.02.014>, 2008
- 9 Tilstra, L. G., O. N. E. Tuinder, and P. Stammes, GOME-2 Absorbing Aerosol Index: statistical analysis, comparison to  
10 GOME-1 and impact of instrument degradation, in *Proceedings of the 2010 EUMETSAT Meteorological Satellite*  
11 *Conference*, EUMETSAT P.57, ISBN 978-92- 9110-089-7, Cordoba, Spain, 2010
- 12 Tilstra, L. G., M. de Graaf, I. Aben, and P. Stammes, In-flight degradation correction of SCIAMACHY UV reflectances and  
13 Absorbing Aerosol Index, *J. Geophys. Res.*, 117, D06209, doi: 10.1029/2011JD016957, 2012
- 14 Tilstra, L. G., Tuinder, O., Wang, P. and Stammes, P.: ALGORITHM THEORETICAL BASIS DOCUMENT GOME-2  
15 Absorbing Aerosol Height, SAF/AC//KNMI/ATBD/005, 1.4, Royal Netherlands Meteorological Institute, de Bilt, 32  
16 pp., 2019, [https://acsaf.org/docs/atbd/Algorithm\\_Theoretical\\_Basis\\_Document\\_AAH\\_Apr\\_2019.pdf](https://acsaf.org/docs/atbd/Algorithm_Theoretical_Basis_Document_AAH_Apr_2019.pdf), last access: 15  
17 October 2020.
- 18 Tilstra, L. G., Tuinder, O., Wang, P. and Stammes, P.: PRODUCT USER MANUAL GOME-2 Absorbing Aerosol Height,  
19 SAF/AC/KNMI/PUM/006, 1.1, Royal Netherlands Meteorological Institute, de Bilt, 28 pp., 2020,  
20 [https://acsaf.org/docs/pum/Product\\_User\\_Manual\\_AAH\\_Aug\\_2020.pdf](https://acsaf.org/docs/pum/Product_User_Manual_AAH_Aug_2020.pdf) , last access: 15 October 2020.
- 21 Torres, O., Bhartia, P. K., Herman, J. R., Ahmad, Z. and Gleason, J.: Derivation of aerosol properties from satellite  
22 measurements of backscattered ultraviolet radiation: Theoretical basis, *J. Geophys. Res. Atmos.*, 103(D14), 17099–  
23 17110, doi:10.1029/98JD00900, 1998
- 24 Vaughan, M., K. Powell, R. Kuehn, S. Young, D. Winker, C. Hostetler, W. Hunt, Z. Liu, M. McGill, and B. Getzewich,  
25 “Fully Automated Detection of Cloud and Aerosol Layers in the CALIPSO Lidar Measurements”, *J. Atmos. Oceanic*  
26 *Technol.*, vol 26, pp. 2034–2050, 2009.
- 27 Veefkind, J. P., Aben, I., McMullan, K., Förster, H., de Vries, J., Otter, G., Claas, J., Eskes, H. J., de Haan, J. F., Kleipool, Q.,  
28 van Weele, M., Hasekamp O., Hoogeveen R., Landgraf, J., Snel R., Tol P., Ingmann P., Voors R., Kruizinga B., Vink R.,  
29 Visser H., and Levelt, P.F.: TROPOMI on the ESA Sentinel-5 Precursor: A GMES mission for global observations of  
30 the atmospheric composition for climate, air quality and ozone layer applications, *Remote Sens. Environ.*, 120, 70–  
31 83, <https://doi.org/10.1016/j.rse.2011.09.027>, 2012.
- 32 Voudouri, K. A., Siomos, N., Michailidis, K., Papagiannopoulos, N., Mona, L., Cornacchia, C., Nicolae, D., and Balis, D.:  
33 Comparison of two automated aerosol typing methods and their application to an EARLINET station, *Atmos. Chem.*  
34 *Phys.*, 19, 10961–10980, <https://doi.org/10.5194/acp-19-10961-2019>, 2019.
- 35 Wandinger, Ulla and Albert Ansmann. “Experimental determination of the lidar overlap profile with Raman lidar”. In: *Appl.*  
36 *Opt.* 41.3, pp. 511–514. DOI:10.1364/AO.41.000511, 2002

1 Wandinger, U., Freudenthaler, V., Baars, H., Amodeo, A., Engelmann, R., Mattis, I., Groß, S., Pappalardo, G., Giunta, A.,  
2 D'Amico, G., Chaikovskiy, A., Osipenko, F., Slesar, A., Nicolae, D., Belegante, L., Talianu, C., Serikov, I., Linné, H.,  
3 Jansen, F., Apituley, A., Wilson, K. M., de Graaf, M., Trickl, T., Giehl, H., Adam, M., Comerón, A., Muñoz-Porcar, C.,  
4 Rocadenbosch, F., Sicard, M., Tomás, S., Lange, D., Kumar, D., Pujadas, M., Molero, F., Fernández, A. J., Alados-  
5 Arboledas, L., Bravo-Aranda, J. A., Navas-Guzmán, F., Guerrero-Rascado, J. L., Granados-Muñoz, M. J., Preißler, J.,  
6 Wagner, F., Gausa, M., Grigorov, I., Stoyanov, D., Iarlori, M., Rizi, V., Spinelli, N., Boselli, A., Wang, X., Lo Feudo,  
7 T., Perrone, M. R., De Tomasi, F., and Burlizzi, P.: EARLINET instrument intercomparison campaigns: overview on  
8 strategy and results, *Atmos. Meas. Tech.*, 9, 1001–1023, <https://doi.org/10.5194/amt-9-1001-2016>, 2016.

9 Wang, P., Stammes, P., Van Der A, R., Pinardi, G. and Van Roozendael, M.: FRESCO+: An improved O2A-band cloud  
10 retrieval algorithm for tropospheric trace gas retrievals, *Atmos. Chem. Phys.*, 8(21), 6565–6576, doi:10.5194/acp-  
11 8-6565-2008, 2008

12 Wang, P., Tuinder, O. N. E., Tilstra, L. G., De Graaf, M. and Stammes, P.: Interpretation of FRESCO cloud retrievals in  
13 case of absorbing aerosol events, *Atmos. Chem. Phys.*, 12(19), 9057–9077, doi:10.5194/acp-12-9057-2012, 2012

14 Winker, D. M., Vaughan, M. A., Omar, A., Hu, Y., Powell, K. A., Liu, Z., Hunt, W. H. and Young, S. A.: Overview of the  
15 CALIPSO mission and CALIOP data processing algorithms, *J. Atmos. Ocean. Technol.*, 26(11), 2310–2323,  
16 doi:10.1175/2009JTECHA1281.1, 2009.

17 Xu, X., Wang, J., Wang, Y., Zeng, J., Torres, O., Reid, J. S., Miller, S. D., Martins, J. V., and Remer, L. A.: Detecting layer  
18 height of smoke aerosols over vegetated land and water surfaces via oxygen absorption bands: hourly results from  
19 EPIC/DSCOVER in deep space, *Atmos. Meas. Tech.*, 12, 3269–3288, <https://doi.org/10.5194/amt-12-3269-2019>, 2019.

20 Zoogman, P., Liu, X., Suleiman, R. M., Pennington, W. F., Flittner, D. E., Al-Saadi, J. A., Hilton, B. B., Nicks, D. K.,  
21 Newchurch, M. J., Carr, J. L., Janz, S. J., Andraschko, M. R., Arola, A., Baker, B. D., Canova, B. P., Chan Miller, C.,  
22 Cohen, R. C., Davis, J. E., Dussault, M. E., Edwards, D. P., Fishman, J., Ghulam, A., González Abad, G., Grutter, M.,  
23 Herman, J. R., Houck, J., Jacob, D. J., Joiner, J., Kerridge, B. J., Kim, J., Krotkov, N. A., Lamsal, L., Li, C., Lindfors,  
24 A., Martin, R. V., McElroy, C. T., McLinden, C., Natraj, V., Neil, D. O., Nowlan, C. R., O'Sullivan, E. J., Palmer, P. I.,  
25 Pierce, R. B., Pippin, M. R., Saiz-Lopez, A., Spurr, R. J. D., Szykman, J. J., Torres, O., Veefkind, J. P., Veihelmann,  
26 B., Wang, H., Wang, J., and Chance, K.: Tropospheric emissions: Monitoring of pollution (TEMPO), *J. Quant.  
27 Spectrosc. Ra.*, 186, 17–39, <https://doi.org/10.1016/j.jqsrt.2016.05.008>, 2017

**Table 1.** Summary of the GOME-2 instrument main characteristics (\*) GOME-2A tandem operation since 15 July 2013

<b>Instrument / Characteristics</b>	<b>GOME-2 MetOp-A</b>	<b>GOME-2 MetOp-B</b>	<b>GOME-2 MetOp-C</b>
<b>Launch date</b>	19 Oct 2006	17 Sep 2012	7 Nov 2018
<b>Spectral Coverage</b>	240 - 790 nm	240 - 790 nm	240 - 790 nm
<b>Spectral resolution</b>	0.26 - 0.51nm	0.26 - 0.51nm	0.26 - 0.51nm
<b>Spatial Coverage</b>	80 x 40 km 40 x 40 km (*)	80 x 40 km	80 x 40 km
<b>Swath width</b>	1920 km – 960 km	1920 km	1920 km
<b>Equator Crossing Time</b>	09:30 a.m. LT	09:30 a.m. LT	09:30 a.m. LT
<b>Global coverage</b>	3 days (High Res.) 1.5 days (Low Res.)	3 days (High Res.) 1.5 days (Low Res.)	3 days (High Res.) 1.5 days (Low Res.)

**Table 2.** Locations of EARLINET lidar stations order by site, with their geographical coordinates and GOME-2/MetOp cases considered in the validation process

Site	EARLINET code	Altitude a.s.l (m)	Latitude (°N)	Longitude (°E)	Common cases
Athens, Greece	<b>ATZ</b>	212	37.96	23.78	3
Barcelona, Spain	<b>BRC</b>	115	41.39	2.11	32
Belsk, Poland	<b>COG</b>	180	51.83	20.78	26
Bucharest, Romania	<b>INO</b>	93	44.34	26.03	10
Évora, Portugal	<b>EVO</b>	293	38.56	-7.91	5
Granada, Spain	<b>GRA</b>	680	37.16	-3.60	32
Lecce, Italy	<b>SAL</b>	30	40.33	18.10	18
Limassol, Cyprus	<b>LIM</b>	10	34.67	33.04	11
Minsk, Belarus	<b>MAS</b>	200	53.91	27.60	5
Potenza, Italy	<b>POT</b>	760	40.60	15.72	2
Sofia, Bulgaria	<b>SOF</b>	550	42.65	23.38	1
Thessaloniki, Greece	<b>THE</b>	60	40.63	22.95	24
Warsaw, Poland	<b>WAW</b>	112	52.21	20.98	3

1

**Table 3.** List of GOME-2 quality-assurance thresholds applied in the EARLINET comparison

<b>Absorbing Aerosol Index (AAI)</b>	$\geq 2$
<b>Sunglint effect</b>	Use only flag values 0, 1, 4, 8, and 33–63 Do not use flag values 32 or 64 and higher
<b>Spatial criterion</b>	$\leq 150$ km radius from the EARLINET stations
<b>Temporal window</b>	5 hours

**Table 4.** Statistical metrics from the validation between GOME-2 AAH and EARLINET retrieved aerosol layer height

<b>Metric</b>	
Number of collocated cases (no.)	172
Mean difference	-0.18 km
Standard deviation	1.68 km
Min   Max of the differences	-4.91 3.91 km
Median	-0.15 km

**Table 5.** Summary of statistics for the comparisons between GOME-2 AAH and LIDAR ALH for all stations\* sorted by maximum number of collocations found.

<b>EARLINET Station</b>	<b>Statistical parameters [in km]</b>				
	<b>N</b>	<b>Mean absolute Bias</b>	<b>STD</b>	<b>Min</b>	<b>Max</b>
Barcelona	32	<b>-0.35</b>	<b>1.94</b>	<b>-4.66</b>	<b>2.86</b>
Granada	32	<b>-0.63</b>	<b>1.79</b>	<b>-3.65</b>	<b>3.9</b>
Thessaloniki	24	<b>-0.05</b>	<b>1.84</b>	<b>-4.71</b>	<b>3.24</b>
Belsk	26	<b>0.19</b>	<b>1.52</b>	<b>-3.11</b>	<b>3.24</b>
Lecce	18	<b>-0.24</b>	<b>1.14</b>	<b>-3.47</b>	<b>2.05</b>
Bucharest	10	<b>-0.39</b>	<b>1.26</b>	<b>-0.96</b>	<b>2.96</b>
Limassol	11	<b>-0.06</b>	<b>1.64</b>	<b>-2.89</b>	<b>2.80</b>
Évora	5	<b>-0.07</b>	<b>1.95</b>	<b>-1.64</b>	<b>3.31</b>
Minsk	5	<b>0.56</b>	<b>0.61</b>	<b>-0.05</b>	<b>1.51</b>
Athens	3	<b>-2</b>	<b>1.38</b>	<b>-3.6</b>	<b>-1.06</b>
Warsaw	3	<b>1.66</b>	<b>0.53</b>	<b>1.08</b>	<b>2.15</b>
Potenza	2	<b>-1.4</b>	<b>1.1</b>	<b>-0.64</b>	<b>-0.64</b>

\*The station of Sofia has only one collocation, therefore it is not shown

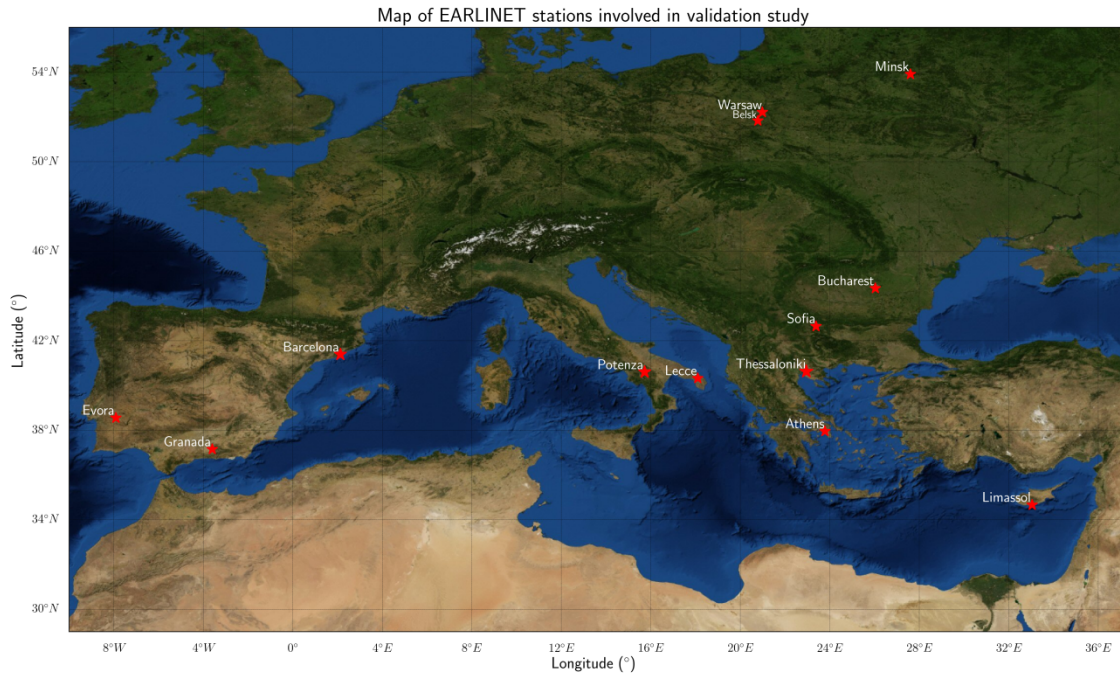


**Figure 1.** Geographical distribution of EARLINET lidar stations used in this study.

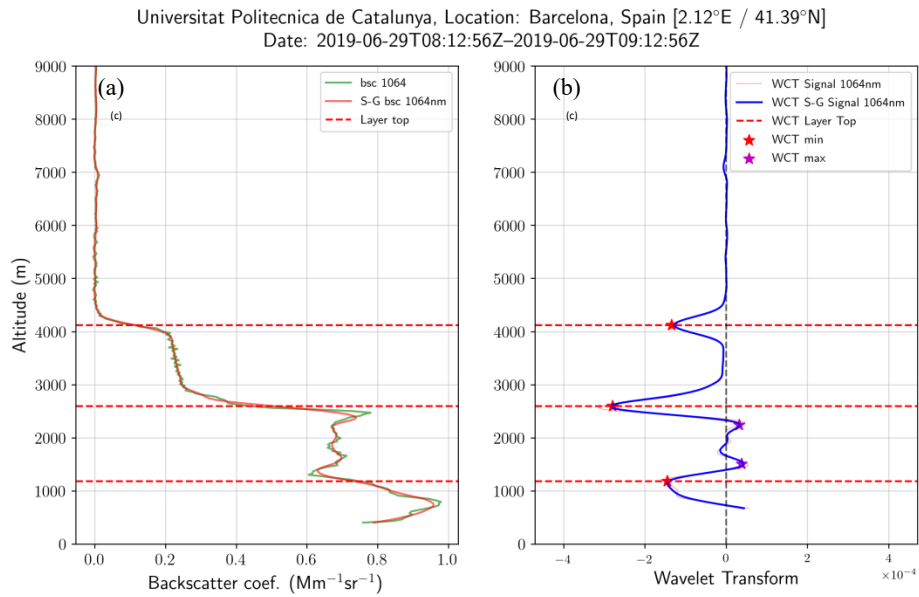


**Figure 2.** Barcelona lidar station (Universitat Politecnica de Catalunya, Barcelona – UPC): (panel a) Lidar backscatter profile at 1064nm and (panel b) resulting WCT profile on June 29, 2019. The horizontal red dashed line represents the detected aerosol layer top applying the WCT methodology. The label “S-G” indicates that a Savitzky-Golay filter was used to reduce to noise variance in the backscatter profile. The colored “star” symbols represent the local maxima (purple) and minima (red) of wavelet transform signal.

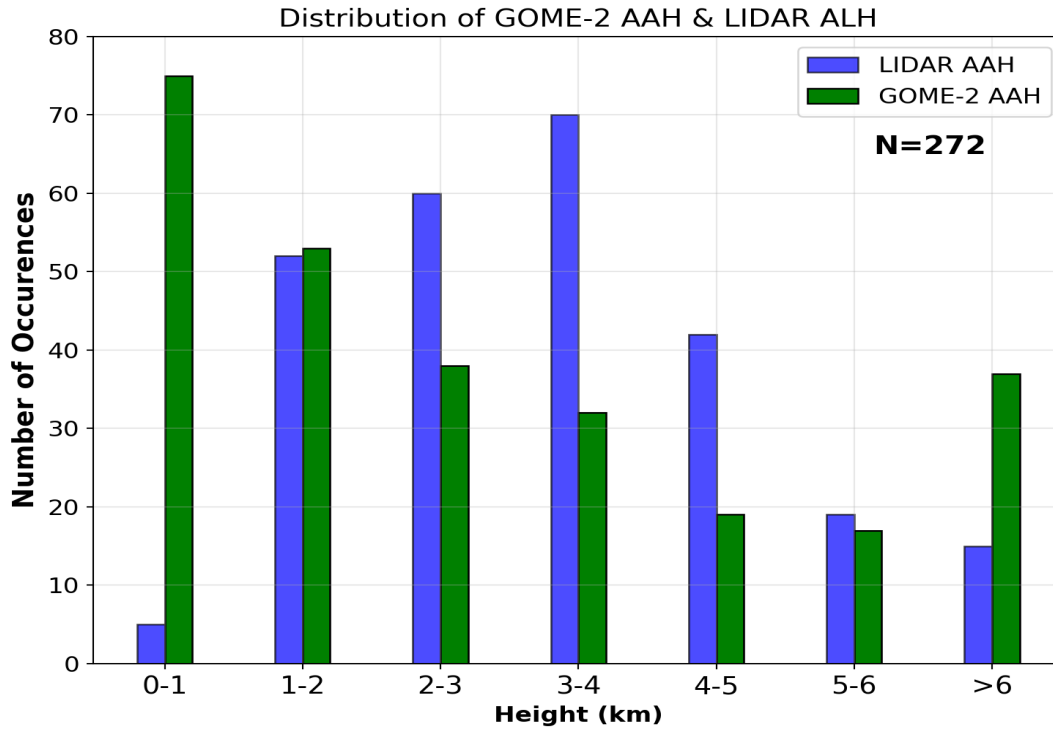


**Figure 3.** Bar plot of GOME-2 AAH (green) and EARLINET ALH (blue) stations. The height ranges of bins are between 0–1, 1–2, 2–3, 3–4, 4–5, 5–6 and > 6 km. The bar counts indicate the number of collocated cases.

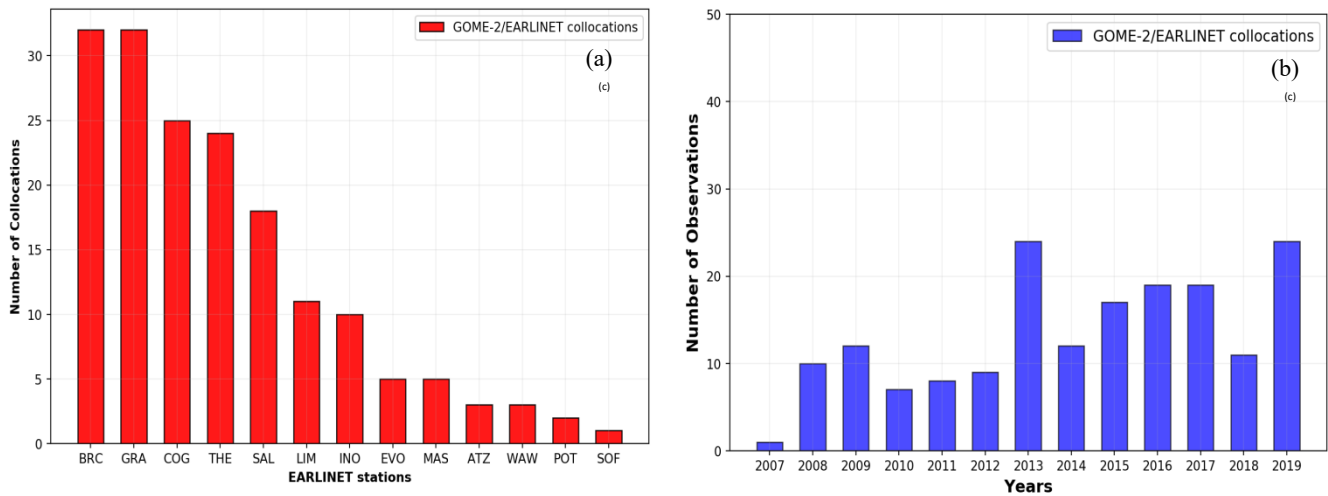


**Figure 4.** Distribution of collocated cases with minimum distance from each lidar station, for a radius distance 150km around each EARLINET station (panel a) and distribution of all collocated cases by year for the study period (2007-2019) (panel b). Refer to Table 2, for the EARLINET code names shown in the x-axis.

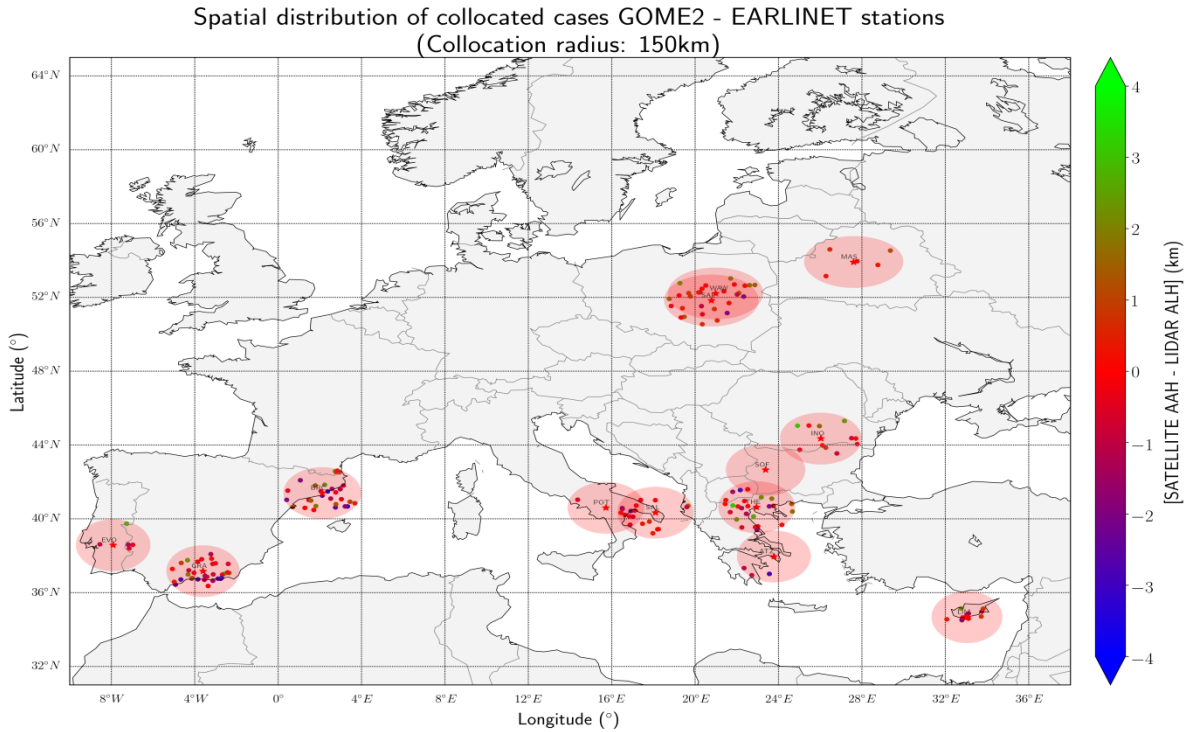


**Figure 5.** Spatial distribution of collocated pairs between GOME-2/MetOp and EARLINET stations for the sites including in the validation study. The color-codes denote the absolute difference between GOME-2/MetOp AAH and the retrieved aerosol height from EARLINET data for each collocated pair. The concentric red circles denote regions of 150 km from the location of EARLINET stations refer to Table 2 for the EARLINET code names shown in the legend.

GOME-2 AAH Regime flag distribution

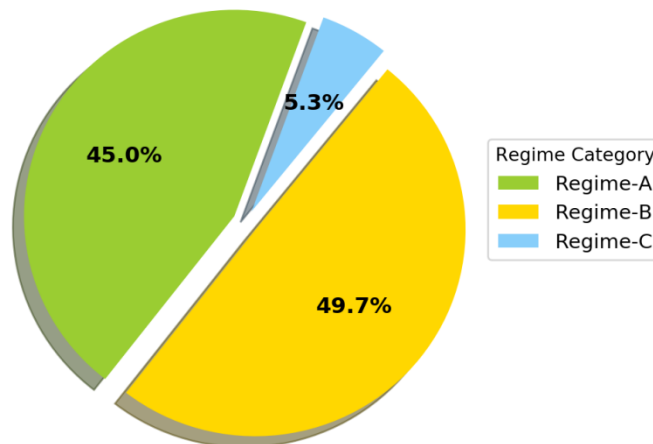


**Figure 6.** Distribution of AAH product reliability (Regime flag) related to degree of cloud cover (effective cloud fraction) for the selected collocated observations as per Sect. 3.1.2. (A: High reliability, B: medium reliability, C: Low reliability)

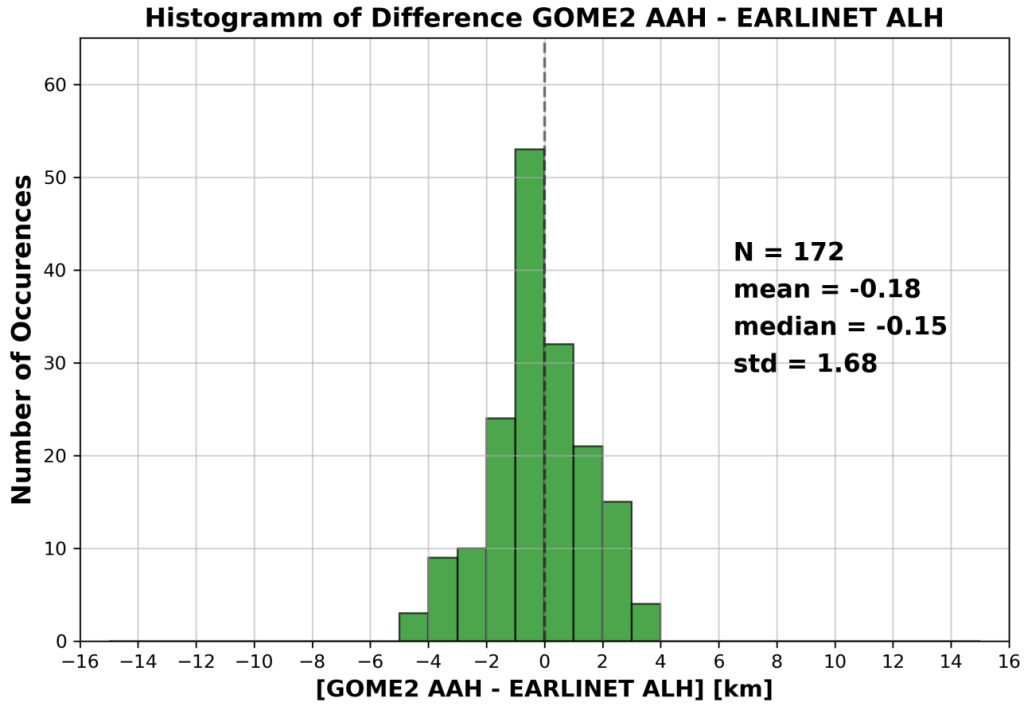


**Figure 7.** Histogram of absolute differences between GOME-2 Absorbing aerosol height and aerosol layer height obtained from EARLINET backscatter profiles (using the WCT method), calculated for all collocated cases.

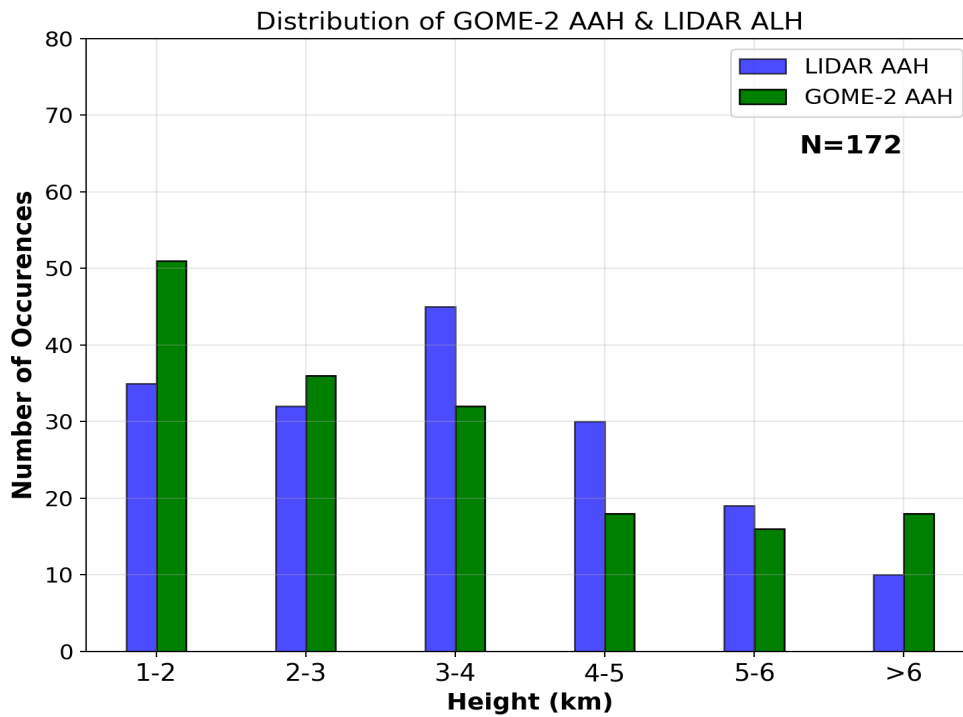


**Figure 8.** Bar plot of GOME-2 AAH (green) and EARLINET ALH (blue) stations occurrences. The height ranges of bins are between 1-2, 2-3, 3-4, 4-5, 5-6 and > 6 km.

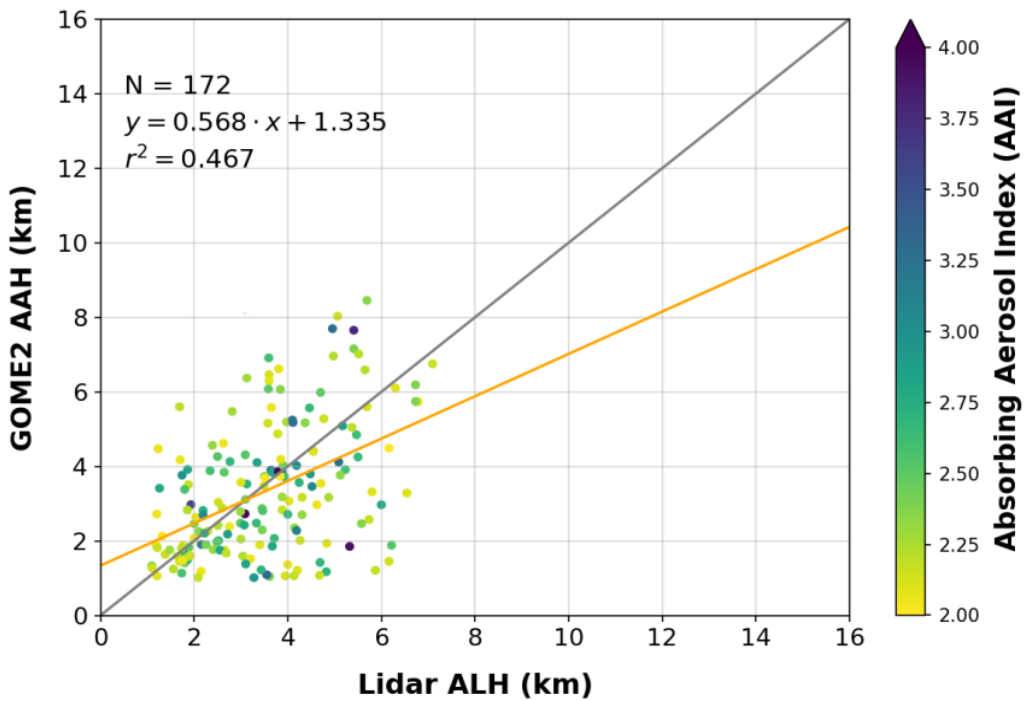


**Figure 9.** Scatterplot between GOME-2 AAH and aerosol layer height from EARLINET stations, for the total of collocated cases. The associated AAI value is color-coded.

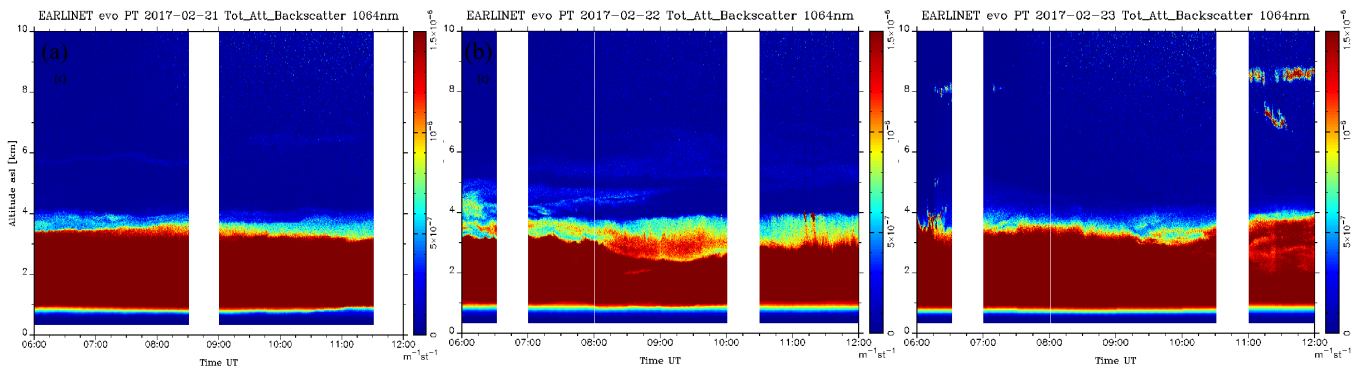


**Figure 10.** Quicklook images corresponding to the total attenuated backscatter at 1064 nm observed with the EARLINET Évora lidar for the 21<sup>st</sup> (panel a), the 22<sup>nd</sup> (panel b) and the 23<sup>rd</sup> (panel c) of February 2017 show nicely the evolution of this particular dust event (<https://quicklooks.earlinet.org/>). (Blue colors indicate weak backscattering signal and yellow and red colors indicate higher backscattering signal).

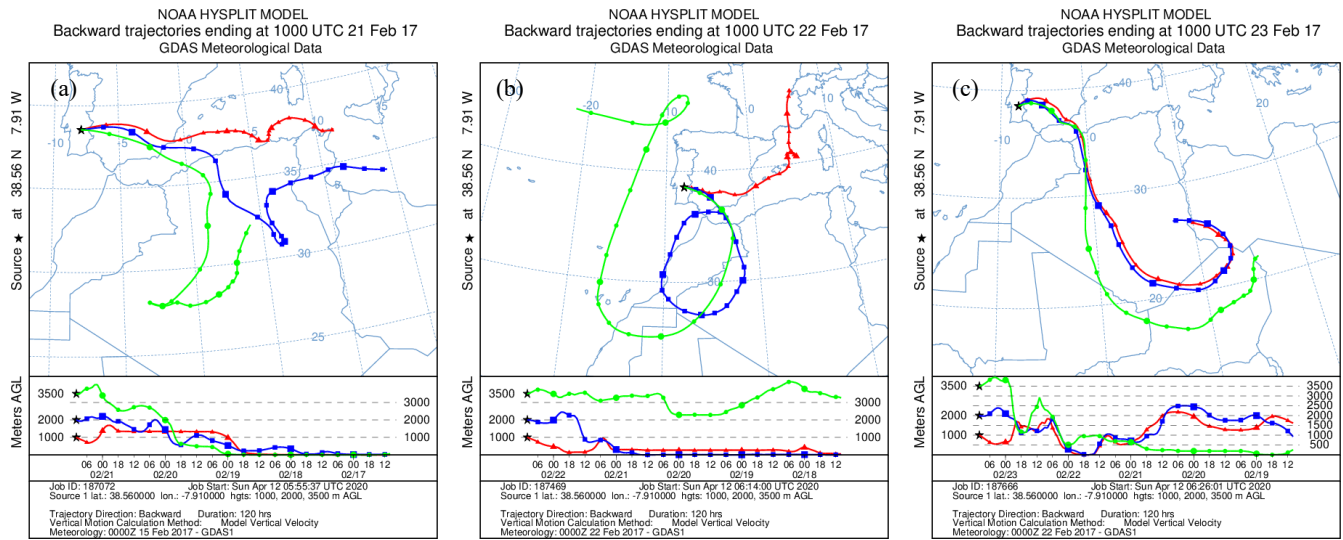


**Figure 11.** The 5-day NOAA HYSPLIT backward trajectories ending at the position of Évora 10:00 UTC (38.56°N, -7.91°E) for the 21<sup>st</sup> (panel a), the 22<sup>nd</sup> (panel b) and the 23<sup>rd</sup> (panel c) of February show nicely the evolution of this particular dust event.

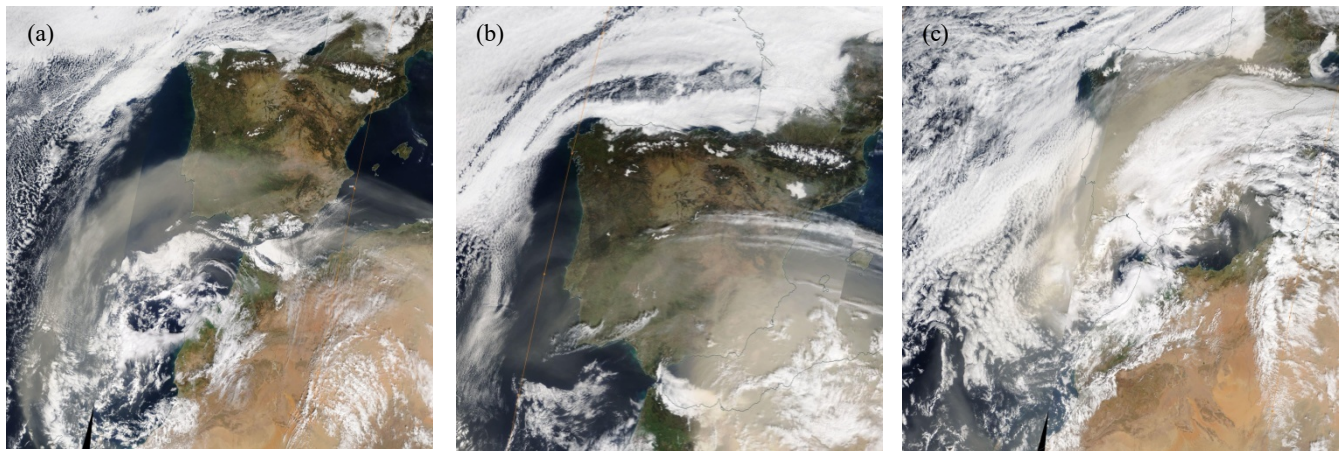


**Figure 12.** Images of Saharan dust transport as captured by the MODIS/Terra satellite, on the 21<sup>st</sup> (panel a), the 22<sup>nd</sup> (panel b) and the 23<sup>rd</sup> (panel c) of February 2017, over the Iberian Peninsula. The orange line denotes the Terra overpasses on the 21<sup>st</sup> (~11:00), 22<sup>nd</sup> (~12:00) and 23<sup>rd</sup> (~11:00) of February 2017 (<https://worldview.earthdata.nasa.gov/>).

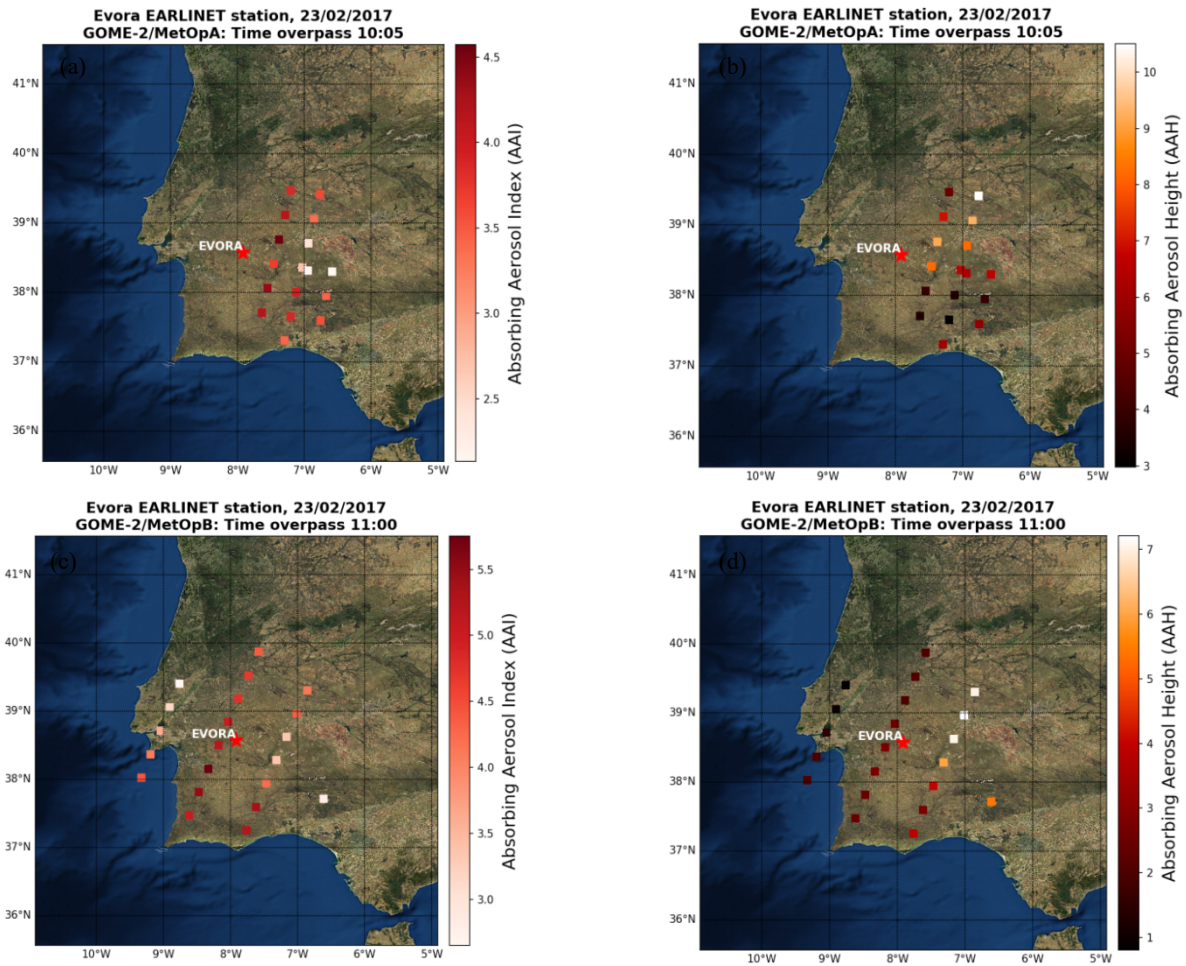


**Figure 13.** The Saharan dust transport on the 23<sup>rd</sup> of February 2017 over the Iberian Peninsula. The Évora station is marked with the red star. The colour schemes illustrate the altitude of the AAH (panel b-d) and the AAI (panel a-c) as observed by GOME-2A (panel a-b) at 10:00 UTC and GOME-2B (panel c-d) at 11:00 UTC.

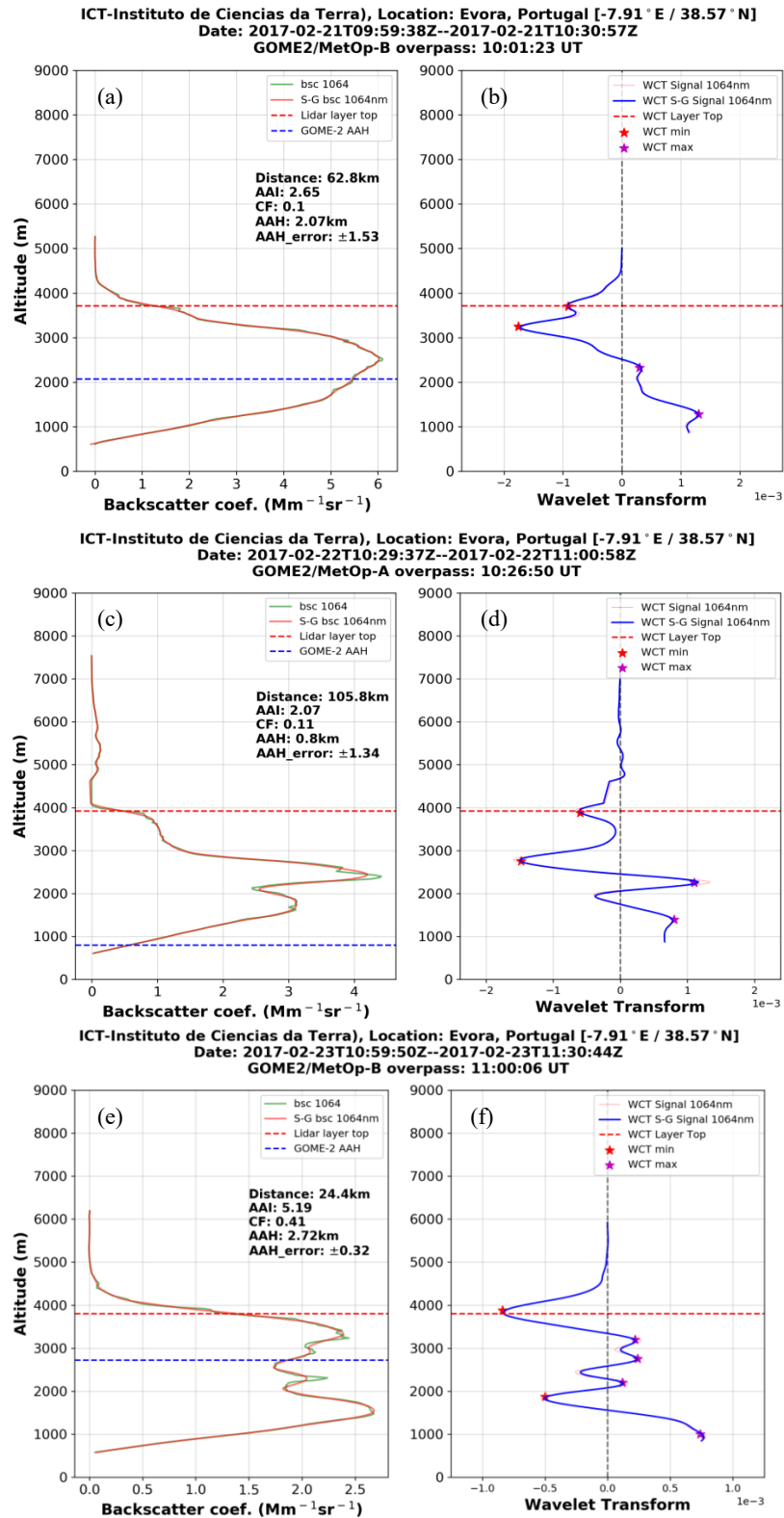


**Figure 14.** Évora lidar backscatter profiles (red and green lines, a, c and e subpanels) and WCT method applied at 1064nm (stars, b, d and f subpanels) and GOME-2A, GOME-2B AAH (blue dashed line) and associated error, AAI, CF and distance (legend) for the 21<sup>st</sup> (panel a-b), the 22<sup>nd</sup> (panel b-c) and the 23<sup>rd</sup> (panel e-f) of February.

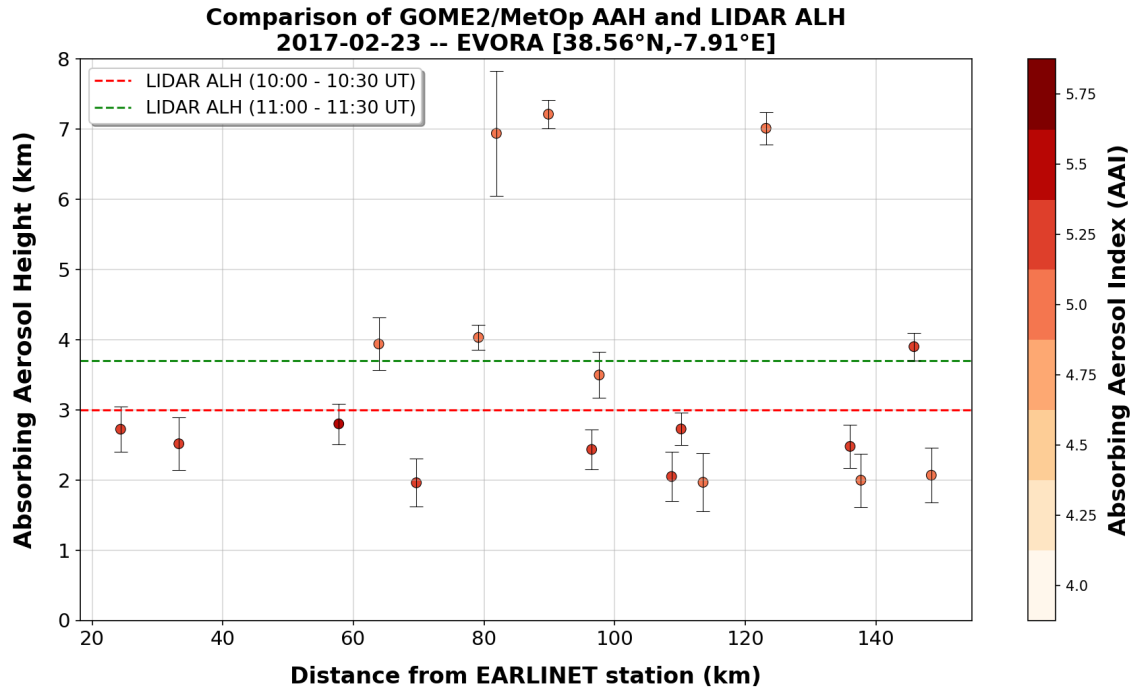


**Figure 15.** GOME-2 AAH (colored dots) against the distance of the retrieved pixels from Évora lidar station, on the 23rd February, 2017. The color scale on the right indicates the Absorbing Aerosol Index (AAI) for GOME-2 pixels. The two dashed lines correspond to the simultaneous lidar observations at 10:00-10:30 UT (red) and 11:00-11:30 (green)